Construction and Building Materials 263 (2020) 120132

Contents lists available at ScienceDirect

Construction and Building Materials

journal homepage: www.elsevier.com/locate/conbuildmat

Interface bond behavior of tensioned glass fiber-reinforced polymer (GFRP) tendons embedded in cemented soils

C. Chen [a,b], G. Zhang [c,*], J.G. Zornberg [d], A.M. Morsy [e], J. Huang [a,b]

[a] *Key Laboratory of Building Safety and Energy Efficiency of the Ministry of Education, Hunan University, Changsha, Hunan 410082, PR China*
[b] *College of Civil Engineering, Hunan University, Changsha, Hunan 410082, PR China*
[c] *College of Civil Engineering, Hunan City University, Yiyang, Hunan 413000, PR China*
[d] *Department of Civil, Architectural and Environmental Engineering, The University of Texas at Austin, Austin, TX 78712, USA*
[e] *Department of Civil Engineering, Cairo University, Giza 12613, Egypt*

HIGHLIGHTS

- A specially designed testing setup and protocol for interface characterization of GFRP tendons embedded in cemented soils.
- A prediction model for interface bond strength based on the dosage and curing time of cemented soils.
- A bond-slip model capable of characterizing interface strength mobilization.

ARTICLE INFO

Article history:
Received 12 October 2019
Received in revised form 4 February 2020
Accepted 3 July 2020
Available online 18 July 2020

Keywords:
Interface bond strength
Bond-slip model
Element pullout test
Glass fiber reinforced polymer reinforcement
Cemented soil

ABSTRACT

This paper presents, evaluates, and interprets element pullout tests conducted to investigate the interface bond behavior of Glass Fiber-Reinforced Polymer (GFRP) tendons embedded in cemented soils. Pullout tests were conducted in conjunction with unconfined compression tests to characterize the strength of the cemented soils in which GFRP tendons were embedded. The effects of water content, cement content, and curing time of the cemented soil on the interface bond strength were investigated. Bond-slip curves of the tested specimens were developed considering a multi-segment function defined by characteristic points of interface bond stress peaks and troughs. Two sets of bond-slip curves were identified based on behavior trends observed in the residual strength phase. The ultimate bond strength of the GFRP tendons in cemented soils was found to strongly correlate with the compressive strength of the cemented soil. Ultimately, the bond-slip behavior was modeled using the cemented soil's unconfined compressive strength and the GFRP tendon's rib spacing. The proposed bond-slip model was developed using correlations of bond strength and against the parameters governing the behavior of cemented soil.

1. Introduction

Cemented soils are used extensively in ground improvement and slope stabilization applications, as they enhance the shear strength and stiffness of natural soils [1,2]. Additionally, uniformly dispersed fibers [3,4] and structural members [5–7] have been typically added to cemented soils to incorporate added tensile capacity to these cementitious composites. Structural members, such as steel reinforcement bars, tubes and steel beams that have been commonly used in reinforced cemented soil systems aim at resisting external tensile loads in a similar manner as reinforced concrete or grouted anchors [6]. That is, by relying on the bond strength between the reinforcement and cemented soil matrix [6,8]. To address concerns associated with corrosion-induced degradation of steel reinforcements embedded in concrete or grout, a number of research studies were carried out to investigate the use of Fiber-Reinforced Polymer (FRP), instead of steel, as reinforcement material in reinforced concrete structures [9–16], anchored and soil nailed systems involving grout bond approaches [17–25] as well as anchored soil systems involving adhesive bond approaches [26–29].

The utilization of steel as reinforcement in cemented soils should address the concern of degradation by corrosion, especially when used in permanent reinforced cemented soil structures [6]. Reinforcements made of different FRP materials have offered a versatile substitute for steel by exhibiting engineering properties that are particularly suitable to reinforced cemented soil structures.

---

[*] Corresponding author.
E-mail address: gbzhang@hnu.edu.cn (G. Zhang).

https://doi.org/10.1016/j.conbuildmat.2020.120132

However, to the authors' knowledge, no research has been conducted on the bond behavior of FRP reinforcements embedded in cemented soils. This has hindered the use of FRP reinforcements in cemented soils in practice.

Several fiber types have been commonly used to produce specific FRP forms, such as Glass Fiber-Reinforced Polymer (GFRP), Carbon Fiber-Reinforced Polymer (CFRP), Aramid Fiber-Reinforced Polymer (AFRP) and Basalt Fiber-Reinforced Polymer (BFRP). GFRP has been preferred in engineering practice due to its satisfactory performance and relatively lower cost as compared to other FRP types [12,19,24,30]. The strength of a cemented soil reportedly depends on the water-cement ratio, and curing conditions and duration [4,31–33].

This paper presents a comprehensive experimental investigation on the bond behavior of GFRP tendons in cemented soils using an element pullout setup [34], which was adopted successfully to test steel rebar-cemented soil interface bond behavior [7]. Results obtained from tests conducted using cemented soil mixes of various cement contents, water contents, and curing durations were evaluated and interpreted to study the effect of each of these three primary variables on the soil-reinforcement bond behavior. Finally, the paper introduces a soil-reinforcement interface bond-slip model calibrated using the obtained experimental data.

2. Testing program

Cemented soils commonly used in engineering practice involve water-cement ratios ranging from 5% to 30% to facilitate a balance between mixture workability and stabilizing effectiveness [1,2]. The cement content adopted in a given project is usually determined by the water content of the natural soils. Soils with a water content below 200% are preferred for the dry mixing method and those with a water content below 60% are preferred for the wet mixing method [2]. Soft soils, which are often stabilized using cement, are often characterized by a natural water content less than 90% or close to the liquid limit [35]. In ground improvement applications, cemented soils tend to develop their full strength after hydration and hardening processes that may exceed a 90-day curing period [36]. Based on these aspects, cement content (C_c), water content (C_w) and curing time (T_c) were adopted as testing variables for the experimental investigation conducted as part of this study. Specimens were prepared with a cement content ranging from 6 to 30%, a water content ranging from 50 to 90%, and curing times ranging from 7 to 90 days. Selection of these ranges aimed at adequately evaluating the effect of the governing parameters on the interface bond behavior of the GFRP Tendon-Reinforced Cemented Soils (GTRCS). It should be noted that the variables evaluated in this study did not include the reinforcement properties since the same type of GFRP tendon was used throughout the testing program.

The three variables selected for the testing program were each assigned different levels within respective ranges, as presented in Table 1. Uniform intervals between levels were implemented for the cement content and water content, whereas linearly increasing intervals between levels were used for curing time because of the nonlinear trend of strength increase for cement-stabilized soils [37]. Accordingly, it was determined that 150 GTRCS specimens were needed to execute the testing program using the three testing variables (5 levels for $C_c \times 5$ levels for $C_w \times 6$ levels for T_c). Note that full experimental design was used in this test to combine test variables with respective levels aiming at attaining adequate test data to perform regression with more reliable correlations than that with limited test data using optimized experimental design methods. Each specimen was designated by the combination of magnitudes of the testing variables; for example, specimen C12W60T14 refers to the GTRCS specimen prepared at 12% C_c, 60% C_w and a 14-day T_c. To evaluate the effect of the cemented soil compressive strength on the interface behavior, cubic specimens of the cemented soils were prepared and tested in compression at the same testing conditions (at the same C_c, C_w, and T_c) corresponding to each GTRCS specimen. Consequently, two types of specimens were prepared for each testing condition (i.e., at each combination of testing variables) in the testing program: the type of GTRCS specimen for pullout testing and the type of cubic cemented soil specimen for compression testing.

3. Material properties

The soil types favorable for introducing hardening agents (cement, lime, silicate-based gel, and chemical solution) to form stabilized ground were characterized by relatively low organic content (typically less than 6%), and high natural water content, e.g. less than 200% for dry method of deep mixing [2]. It is noteworthy that the above soil conditions favorable for soil mixing application were identified to be unfavorable for conventional soil nailing practice due to its high plasticity and low bond resistance [38]. However, the integration of soil mixing and soil nailing technique made the above soil conditions the most suitable and favorable for the application of reinforced cemented soils, e.g. soil mixing anchor and stiffened deep mixing column [2,6]. Hence, the high-plasticity clays were typically used throughout the testing program which were deemed an idea representative for the soils in universal common practice of reinforced soil mixing [6]. The soil samples used in this testing program were collected from the floodplain in the vicinity of the intersection of the Xiangjiang River and Jinjianghe River in the City of Changsha, China, as shown in Fig. 1. This floodplain is characterized by a vast presence of high-plasticity soft clays, with natural water contents exceeding 80% in some locations. This floodplain is characterized by a vast presence of high-plasticity clays, with natural water contents exceeding 80% in some locations. The basic properties of the soil samples were obtained in the laboratory, as presented in Table 2. Soil samples were air-dried in a laboratory environment and mechanically pulverized, with only particles passing the 5-mm sieve being used for sample preparation aiming at attaining reasonable uniformity for clay samples. The particle-size distribution of the soil samples used in the cemented soil mixtures is presented in Fig. 2. GFRP tendons were used as reinforcement in the GTRCS pullout specimens. The cement used in the cemented soil mixtures was conventional Portland cement. Both the GFRP tendon and cement are commercially available and their properties, as provided by the manufacturers, are shown in Table 2.

Table 1
Testing variables and respective levels adopted in testing program.

Testing variables	Number of levels	Magnitude of levels					
Cement content C_c (%)	5	6	12	18	24	30	
Moisture content C_w (%)	5	50	60	70	80	90	
Curing time T_c (day)	6	7	14	28	42	60	90

Fig. 1. Aerial photograph showing the location of floodplain where soil samples were collected.

Table 2
Information of materials used throughout testing program.

Properties	Values / Description
Soil	
Natural water content (%)	30–90
Liquid limit (%)	58.1
Plasticity limit (%)	28.6
Specific gravity	2.705
Cement	
Type	P.O 42.5
Compressive strength (MPa)	≥42.5 (28-day)
Reinforcement	
Type	GFRP tendon
Outer diameter (mm)	16.8
Inner diameter (mm)	15.0
Rib spacing (mm)	10.1
Tensile strength (MPa)	466
Young's modulus (GPa)	40

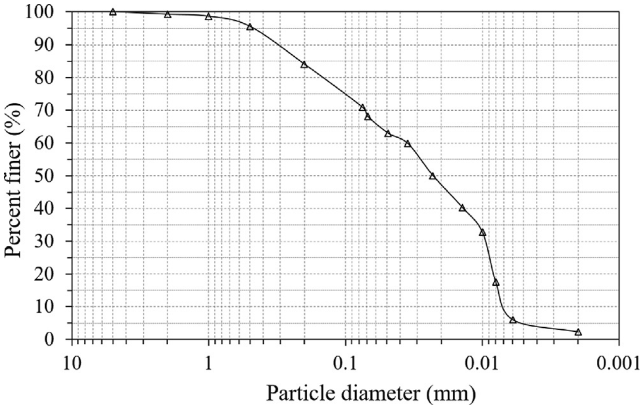

Fig. 2. Particle size distribution of soil sample.

4. Experimental methodology

4.1. Testing devices

The GTRCS specimen was characterized by a small bond length between the GFRP tendon and cemented soil corresponding to a unit cell (or element physical model) of a typical soil mixing anchor. Accordingly, a segment of an actual field anchor involved a cylindrical specimen, with the tendon centered in the cemented soil mass. The bond length of the GFRP tendon specimen was set at 80 mm, or five times the diameter of the tendon. According to the reported bond characterizations of concrete reinforcing bars [8], rockbolts [39,40] and epoxy adhesive anchors [41], segments with such bond lengths can generate approximately uniform distributions of interface bond stresses throughout the interface area of tendons subjected to the pullout force. Based on observations and findings of single pile settlement testing and analyses [42,43], the diameter of the cemented soil must exceed 10 times the tendon diameter to allow for adequate transfer of the shear stresses generated at the interface into the cemented soil and minimize the specimen boundary effect on test results. It should be noted that, referring the bond test setup for reinforced concrete and rockbolt [8,38] the confinement of the tendon in this pullout cell was simulated by the hardening process of cemented soils instead of normal stress boundary applied to the specimen periphery. The pullout cell, illustrated in Fig. 3, was specifically designed to account for the aforementioned considerations while facilitating specimen preparation.

Short housing sleeves were attached to the cover and base plates in the cell to isolate the cemented soils and tendon, ensuring uncoupled soil-tendon interface at ends of the cell. The uncoupled portion at the loaded end (cover plate) aims at effectively mitigating stress concentrations in the vicinity of the interface, and the uncoupled portion at the free end (base plate) aims at maintaining a constant interface shear area during the pullout process. The diameter of the hole on the cover plate is larger than the tendon diameter solely to minimize any offset in tendon location from the center. Consequently, the cover plate was halved to facilitate placement of the tendon.

The pullout load was applied to the tendon of the GTRCS specimen using a Pile/Anchor Interface Friction Testing System (PIFTS), which was developed specifically to accommodate element pullout specimens [44–46]. The effectiveness of the PIFTS has been validated in interface behavior characterizations for grouted anchor elements in soils and rebar-reinforced cemented soil specimens [7,34,47]. The setup of the PIFTS is shown in Fig. 4. The GTRCS specimen was placed and mounted on the platform with the tendon's head connected to the load cell. The pullout force is applied to

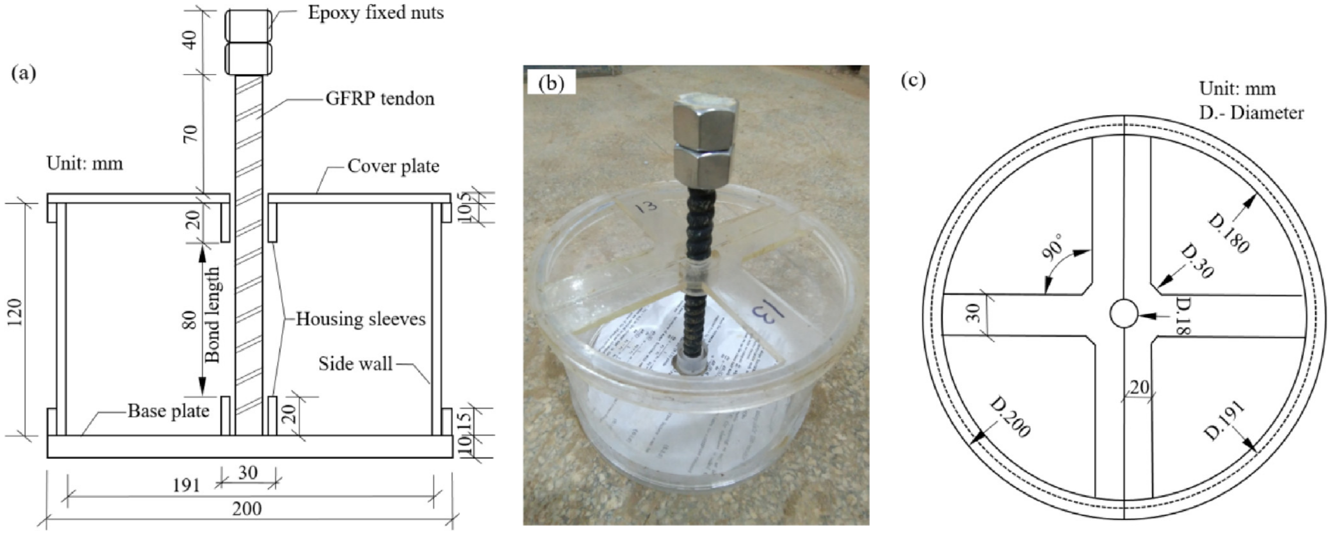

Fig. 3. Setup of pullout cell: (a) schematic of cross-sectional elevation; (b) 3D view of cell; and (c) schematic of cross-sectional plan.

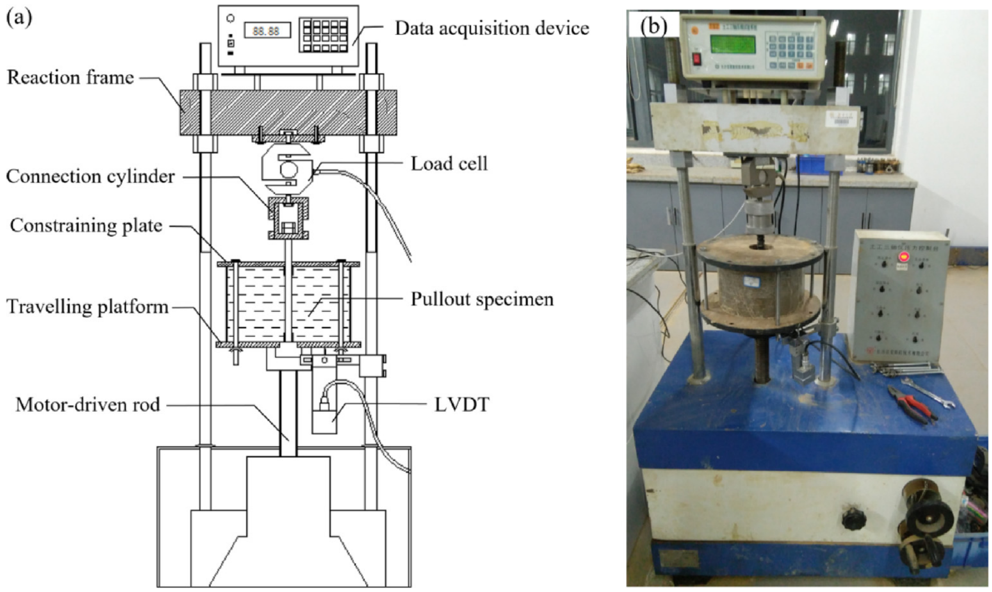

Fig. 4. Pullout loading device: (a) schematic of setup; and (b) view in lab.

the tendon by lowering the platform on which the GTRCS specimen is mounted. The pullout force and traveling displacement were monitored and recorded in real-time by a data acquisition system.

Furthermore, a compatible connection was needed to mount the tendon's loaded end to the load cell in the PIFTS. The loaded end of the tendon was enlarged by two stacked nuts, fixed with epoxy resin, forming an augmented load head, as shown in Fig. 3a. A compatible hollow cylinder connection, shown in Fig. 5, was used to attach the tendon's loaded head to the load cell. The cylinder was spilt in two along its vertical axisymmetric plane, with a central hole on its top and base. The tendon's head was locked into the cylinder by combining the two parts with the screw ring. The load cell was then connected to the cylinder using a threaded rod, with one end screwed into the base hole of the load cell and the other end locked into the cylinder with nuts. All screw connections were carefully designed to account for the appropriate capacity for the maximum pullout load range.

To characterize the effect of the multiple relevant properties on the interface behavior, the compressive strength of the cemented soils used in the pullout specimens was obtained via unconfined compression tests. Cubic specimens of the cemented soils were tested using the two compression machines shown in Fig. 6: (a) CMT4202 is a computer-controlled general testing machine with a capacity of 19 kN and a precision of 0.001 kN; and (b) TYE600B is a compression machine with a capacity of 600 kN and a precision of 0.01 kN. Because the strength of the cemented soils tested in this program was wide-ranging, the two compression machines pictured in Fig. 6 were used to facilitate a consistent precision/capacity ratio in measurements.

4.2. Specimen preparation

GTRCS specimen tendons were 330 mm in length and connected to two nuts with epoxy resin at the loaded end, as shown in Fig. 7. The bond strength of this adhesive was evaluated, confirming that no shear displacement occurred along the nuts at loads corresponding to the maximum loads expected in the GTRCS pullout testing program. Tendon specimens were installed in the

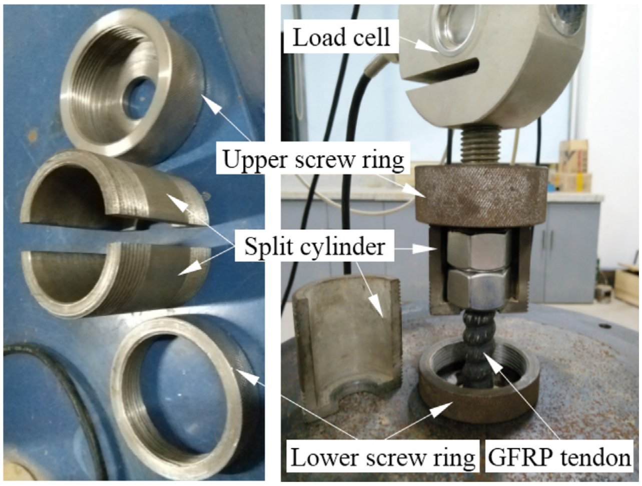

Fig. 5. Setup of connection cylinder.

center of the pullout cell prior to placement of the cemented soils (Fig. 3b).

Soil and cement were mixed with an agitator in a dry condition for 60 s in specific quantities, to reach the target testing variables (C_c, C_w, and T_c) in Table 1. The respective volume of water was added to the agitator, which continued mixing for 480 s. This dry-wet mixing sequence was found to minimize moisture losses while achieving effective mixing. The duration of wet mixing was extended for specimens with very low water content, but it did not exceed 750 s. The mixed cemented soils were transferred to the pullout cell (for one GTRCS specimens tested in pullout) and cubic cell (for three specimens tested in unconfined compression). It is noted that cubic cell with edge length in 7 cm was used herein in accordance with concrete strength testing protocol to facilitate the compressive strength measurement of cemented soils. The bases of both cells were covered with paper plate sealants to prevent the loss of cemented soils. The inner surfaces of the cells in contact with the cemented soils were lubricated to minimize boundary friction. Both cells were placed and vibrated on a vibration table to densify the specimens and attain a uniform density, especially near the tendon surface. Following vibrating densification, the cells were placed in zip-top plastic bags to cure the cemented soil mixtures for the respective predetermined curing period. After the seven-day early hardening of the cemented soils, the cover plate and base plate of the pullout cell were removed to prevent excessive adhesion between the plates and cemented soils that could develop during curing. Preparation of pullout and cubic specimens was completed following demolding from the cells at the end of the curing period.

4.3. Testing procedures

Pullout specimens were installed in the PIFTS by connecting the tendon head to the load cell and mounting the specimen to the traveling platform, as shown in Fig. 4b. The constraining plate and traveling platform were screwed together securely to allow for compatible interface shear displacement with the downward movement of the platform. The lowering of the traveling platform was set at a displacement rate of 1.0 mm/min to convey a displacement-controlled pullout loading to the GFRP tendon. Loading was terminated when the platform displacement reached 20.0 mm, which was found to adequately result in a complete de-bond between the tendon and encapsulating cemented soils [7,34]. The pullout force and platform displacement monitored by the load cell and Linear Variable Differential Transformer (LVDT), respectively, were recorded in real-time and used to interpret the uniformly distributed interface bond stress and interface slip as assumed in the element pullout test concept discussed earlier.

The cubic specimens (three in a group) were prepared at the same conditions as the pullout specimens and tested in unconfined compression to measure the compressive strength of the cemented soils at the various combinations of testing variables (C_c, C_w, and T_c). The compressive strength of the cubic specimens was initially estimated using the strength development model of cement-stabilized soils reported in Åhnberg 2006 [37]. The cubic specimens with estimated strength greater than 20 kN were tested using TYE600B (Fig. 6b), and those with estimated strength below 20 kN were tested using CMT4202 (Fig. 6a). The loading rates used in the compression tests ranged from 0.01 to 0.20 kN/second

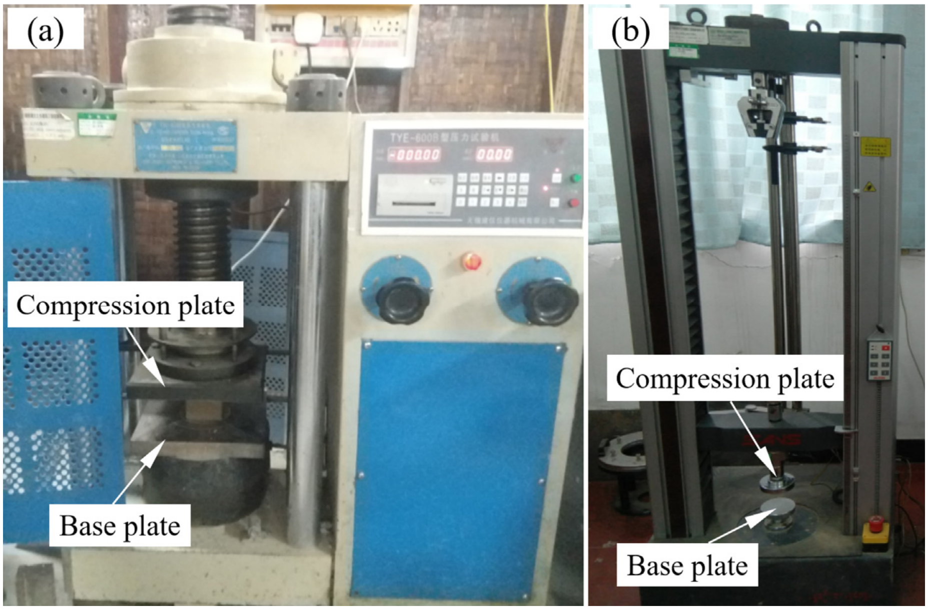

Fig. 6. Unconfined compression machines: (a) CMT4202; and (b) TYE600B.

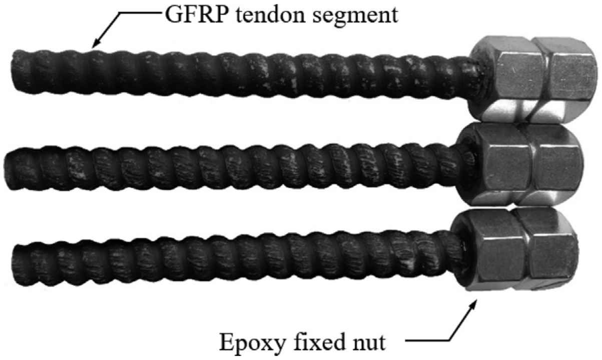

Fig. 7. View of completed GFRP tendon specimen.

according to the respective estimated strength of the specimen. The measured compressive forces were manually recorded throughout the compression tests. The peak compressive force was averaged over the contact area between the cubic specimen and compression plate to represent the unconfined compressive strength of the cubic specimen.

5. Testing results

After completion of the pullout tests, specimens were dissected and GFRP tendons were exhumed. All exhumed tendons were found to have cemented soil wedges attached at the loaded end of the bond length, as shown in Fig. 8a, indicating that pullout occurred because of shear failure of the cemented soils rather than interface bond failure. It is noteworthy that the width of each wedge was precisely equivalent to the outer diameter of the pullout cell housing sleeve, as shown in Fig. 3a. A gap between the tendon and cemented soil was observed when the housing sleeve was removed with the cover plate during the curing period. This unconstrained gap produced the cemented soil wedge prior to the interface bond resisting the pullout force. The effective bond length for each pullout specimen was defined by subtracting the wedge height (denoted by h_{wed}) as measured from the exhumed tendons, as presented in Appendix A.

Significant stripes were observed on the cemented soil interfaces, and the spaces between neighboring tendon ribs were filled with cemented soil, as pictured in Fig. 8b. The interface bonding mechanism involves a combination of soil cohesion over the tendon surface, friction between soils and tendon surfaces and occlusion between soils and ribs, which led to the development of a shear band in the cemented soil zone close to the interface. The geometry and width of this shear band was difficult to measure in the testing setup used in the present investigation, which also made determination of the shear interface area impractical. Based on the commonly used idealization of the bond area between reinforcement and cemented soil matrix [7,34,38], the nominal diameter of the tendon was used to characterize the bond interface, which was 16 mm in this testing program. Accordingly, the interface bond area of the pullout specimen was simplified as the product of the tendon's nominal perimeter and the effective bond length as stated previously. Consequently, the pullout forces monitored in the loading process were averaged over the effective bond area to characterize the interface bond stresses for each pullout specimen.

Additionally, the monitored displacements of the traveling platform were corrected by subtracting the tensile elongations of the free segment for the tendon subjected to the pullout forces. Because the deformation of the cemented soils for each pullout specimen was constrained within the cell, it was reasonable to use the corrected displacement of the platform to characterize the relative displacement as uniform along the length of the interface in the element specimen (i.e., characterizing the interface slip).

Appendix B presents the bond-slip curves for all 150 pullout specimens tested in this investigation, as well as figures containing curves for tests conducted on specimens prepared with the same water-cement ratio and varying curing times.

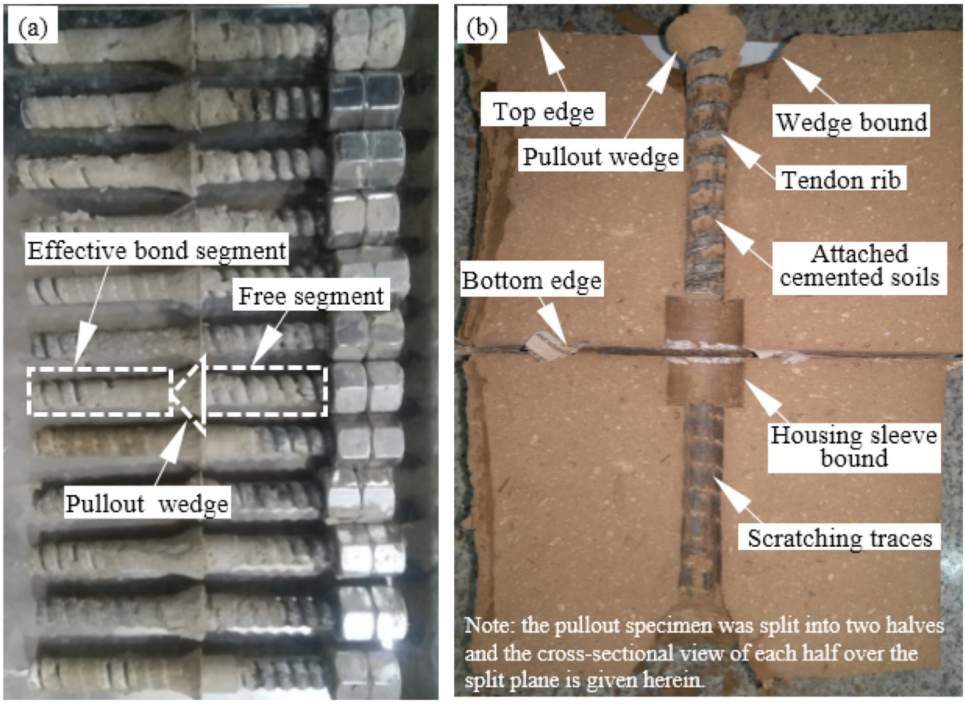

Note: the pullout specimen was split into two halves and the cross-sectional view of each half over the split plane is given herein.

Fig. 8. View of pullout specimen after dissection: (a) view of typical retrieved GFRP tendons with attached wedges; (b) view of typical interface on the cemented soils.

These bond-slip curves were classified according to their morphological characteristics into two general sets with typical features, which are referred to herein as the waved and still sets, as shown in Fig. 9. The curves in both sets were characterized by three phases: a linear phase, a strain softening phase and a residual phase. The linear phase corresponds to an approximately linear initial portion of the curve; the strain softening phase involves a decrease in bond stress beyond the peak stress value, characterized by a decreasing slope with increasing interface slip; and the residual phase showing a stabilized bond stress with increasing slip magnitudes. In particular, the waved set differs from the still set by the presence of a bond stress fluctuation in the residual phase. Accordingly, the waved set is defined by four characteristic points that correspond to two peak points and two trough points (Fig. 9a). In contrast, the still set is defined by two characteristic points that correspond to one peak point and one residual point (Fig. 9b). It should be noted that the residual point in the still set corresponds to the first trough point in the waved set when the residual phase is free of stress fluctuations.

Based on the characteristic points defined for the two sets, the bond-slip curves of the 150 pullout specimens tested in this study with different combinations of testing variables were distinguished by the bond stresses and slips corresponding to the characteristic points, as listed in Appendix A. It is significant that four specimens with specific testing variables (specimens C24W50T28, C24W50T42, C30W50T14 and C30W50T28) exhibited a failure mode with radial cracks in the surrounding cemented soils, as presented in Fig. 10. It should also be noted that specimens C24W60T60 and C30W60T60 experienced loading interruptions, which resulted in incomplete bond-slip curves after the first peak point.

Unconfined compression tests were conducted on 150 groups of cubic specimens (three specimens per group) in conjunction with the respective pullout specimens as discussed previously. The shear failure of each cubic specimen was observed at an approximately 45-degree failure plane angle to the specimen edge. Only two corresponding specimens were prepared for six groups with very high water content, and measurements were not available for one specimen for five other groups due to technical difficulties experienced in the loading process. Unconfined compressive strengths (UCS) of the remaining 439 cubic specimens are also included in Appendix A.

6. Regression analyses

6.1. Ultimate interface bond strength versus unconfined compressive strength

The bond strength of a steel reinforcement bar embedded in concrete or cemented soil has been reported to be proportional to the unconfined compressive strength of the concrete or cemented soil [7,8]. Regression of mean unconfined compressive strength (UCS_{mean}) and ultimate interface bond strength (τ_{p1}) data generated in this study (Appendix A) suggest a linear correlation, as shown in Fig. 11a.

The correlation indicates that the maximum interface bond strength, which can be mobilized as shear resistance along the GFRP tendon interface, is proportional to the compressive strength of the cemented soils in which the tendon is embedded. Considering data from similar tests conducted by the authors [7] with steel bar reinforcement and the fact that the stiffness of both GFRP tendon and steel bar is substantially greater than that of cemented soils, it is inferred that the slope of the linear correlation depends on the tendon surface geometric properties, including rib dimension and spacing. Specifically, the magnitude of the slope was found to be 0.486 for the GFRP tendon (1.8 mm in rib height and 10 mm in rib spacing) used in this study, while the slope magnitude for the steel bar reinforcement (1.5 mm in rib height and 10 mm in rib spacing) was reported to be 4.02 [7].

6.2. Residual interface bond strength versus ultimate interface bond strength

The residual phase of the bond-slip curve was characterized by a series of peak and trough points, as schematically illustrated in Fig. 9. The residual interface bond strength was defined as the bond stress corresponding to the first trough point of the bond-slip curve, which was identified as the onset of the residual phase. The trough bond strength in the residual phase tends to decrease with increasing slip displacement, and the lowest bond strength (i.e., fully-softened strength) is not expected to have been reached within the range of the slip values achieved in the tests conducted in this investigation. An approach to predict the actual residual bond strength involved using a function to fit the stress fluctuation in the residual phase from which an asymptotic stress can be obtained, which describes the proposed bond-slip model, as will be discussed in the following section. Note that the six specimens that exhibited radial cracks at failure and tests with incomplete bond-slip curve measurements (C24W50T28, C24W50T42, C30W50T14, C30W50T28, C24W60T60 and C30W60T60) produced bond-slip curves that are inconsistent with the remaining 144 specimens, as discussed earlier, and were not used in the derivation of the correlation.

The residual interface bond strength was found to be approximately 0.24 of the ultimate interface bond strength, as shown in Fig. 11b. The soil-reinforcement interface bond strength can be represented by three components: mechanical interlock, interfacial friction, and interfacial cohesion. The mechanical interlock and interfacial cohesion components decreased remarkably from the ultimate bond strength (first peak) to the residual bond strength (first trough). Thereafter, bond strength comprised chiefly of gradually decreasing mechanical interlock and constant interfacial friction. The ratio of the residual to ultimate interface bond strength (i.e., 0.24) indicates that the mechanical interlock contributed substantially (approximately 75%) to the interface bond strength for the typical GFRP tendon used in this study.

6.3. Bond strength threshold for residual stress fluctuation

As discussed earlier, two sets for bond-slip curves were defined in this study: (a) the waved set, characterized by a stress fluctuation in the residual phase (after the first bond stress trough); and (b) the still set, characterized by a flat slip flow (comparatively constant bond stress) in the residual phase. A bond-slip curve set index with values of 1 and 2 were used to represent the still set and waved set, respectively. Fig. 12 shows the set switch with increasing ultimate interface bond strength, where the corresponding switch threshold was found at an approximate ultimate bond strength of 240 kPa. It can be inferred that a residual phase with stress fluctuation would be found in the bond-slip curve for an element pullout specimen with an ultimate bond strength greater than 240 kPa, which corresponds to a GFRP tendon embedded in cemented soil with a compressive strength greater than 494 kPa, according to the correlation in Fig. 11a. Using this strength threshold can facilitate the pick between two sets (waved and still) in modelling the bond-slip behavior of GFRP tendons embedded in cemented soils by solely concerning the compressive strength of the cemented soils as matrix.

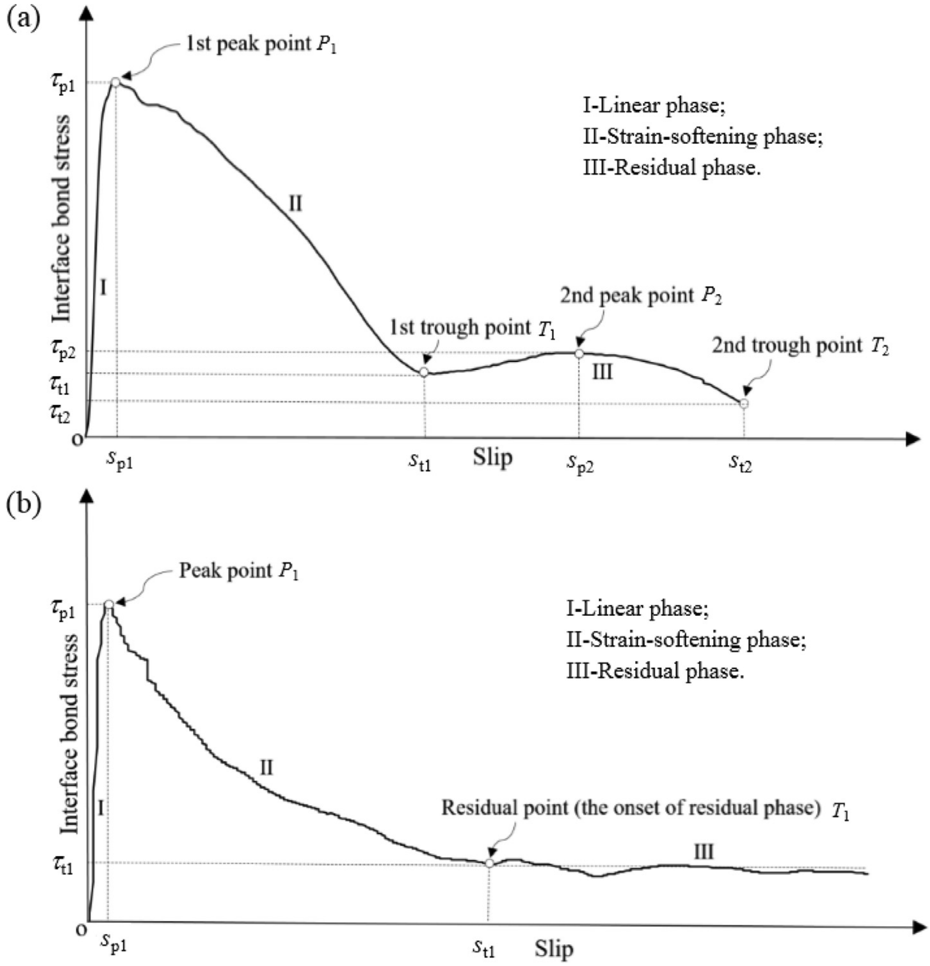

Fig. 9. Schematic of typical sets of bond-slip curves: (a) waved set; and (b) still set.

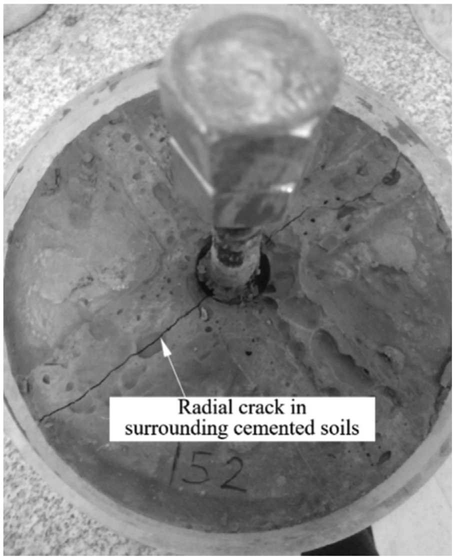

Fig. 10. Typical view of radial crack in surrounding cemented soils.

6.4. Secant stiffness for the linear phase of the bond-slip curve

The linear phase of the bond-slip curve characterizes the shear straining of the tendon interface with the surrounding cemented soil. The secant slope at the first peak point in the bond-slip curve (τ_{p1}/s_{p1}) can be used to define the shear stiffness of the interface (k_{sec}), which can be used to predict the pullout resistance of the tendon embedded in the cemented soils under small pullout displacements. The magnitude of the interface secant stiffness was found to be proportional, when plotted in a logarithmic scale, to the magnitude of the ultimate interface bond strength, as depicted in Fig. 13. The slope of this correlation depends on the tendon surface properties, which are tendon-specific, similar to the coefficients defined by the results presented in Fig. 11. This correlation relates the straining behavior with the strength properties for the soil-reinforcement interface.

6.5. Bond strength at other bond-slip characteristic points

Three characteristic points involved in the residual phase of the bond-slip curve in the waved set include the first trough (the onset of the residual phase), the second peak, and the second trough, as illustrated in Fig. 11a. Because the residual interface bond strength was defined at the onset of the residual phase in both the waved and still sets, a bond stress condition can be suitably defined by correlating the residual and ultimate bond strengths for the still and waved sets. Similar correlations will still be required to define the remaining peak and trough for the waved set. The bond stress data corresponding to the second peak and trough in the residual phase of the waved set were plotted against the ultimate interface bond strength (i.e., bond stress for the first peak) as can be seen in Fig. 14a and b, respectively.

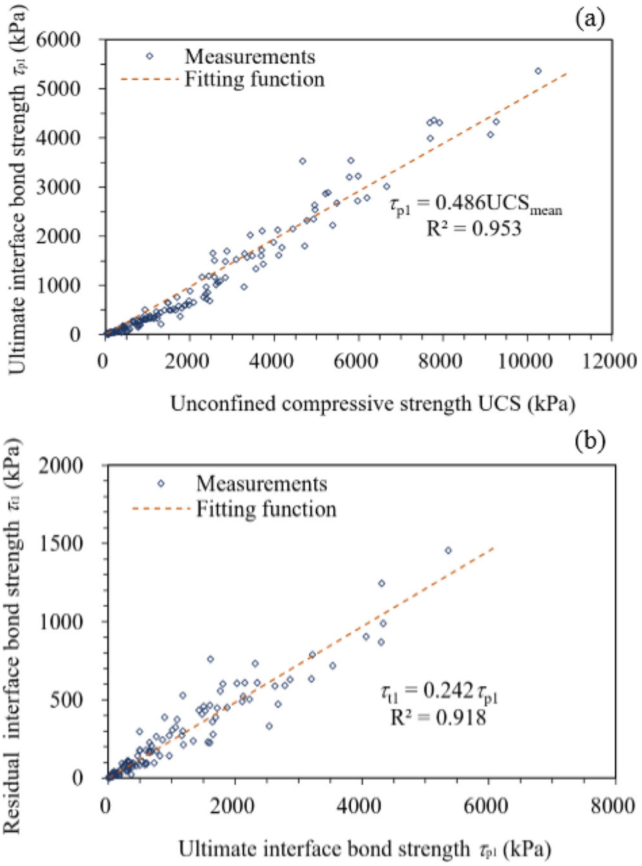

Fig. 11. Correlations among related strengths: (a) soil compressive strength versus ultimate interface bond strength; (b) residual versus ultimate interface bond strength.

Linear regression functions were developed with acceptable determination coefficients (R^2). These functions revealed that the bond strength corresponding to the peak and trough of the residual phase with stress fluctuation could be related to the value of the ultimate interface bond strength by adopting reduction factors. The values of the reduction factors were defined by the slopes of the linear functions, shown in Fig. 14 as 0.36for the second peak and 0.19 for the second trough, respectively. These values are reasonable for the typical GFRP tendon used in this study. The testing data for specimens with incomplete measurements and those that exhibited radial crack failure and/or loading interruptions were not used in the aforementioned regression functions.

6.6. Slip magnitudes for characteristic points in the residual phase

The magnitude of slip corresponding to the first peak (i.e., ultimate interface bond strength) was considered in evaluating the secant stiffness in the elastic phase of the bond-slip curve. Similarly, the magnitudes of slip corresponding to the first trough (for both the waved and still sets), and the second peak and second trough (for the waved set) in the residual phase were assessed together with the tendon's rib spacing, i.e. a typical surface geometric property of the tendon, as seen in Fig. 15.

It was found that the slip magnitude corresponding to the onset of the residual phase for all specimens was consistent with the magnitude of the rib spacing of the GFRP tendon (10 mm), averaging 9.21 mm. Also, the slip magnitude corresponding to the second trough was found to be consistent with (although slightly smaller than) twice the magnitude of the tendon rib spacing (20 mm), with an average value of 18.66 mm. The slip distribution related to the second peak was observed to be approximately equivalent to the average of the aforementioned two slip magnitudes (15 mm), with an average value of 13.29 mm. The slip range between the origin and the first trough was found to be greater than the slip range between the first and second troughs, which indicates that the "wave length" decrease manifested in the bond-slip curves of the waved set. An explanation of the reduced "wave length" is given in the following section on interface shear strength mobilization.

6.7. Ultimate interface bond strength versus testing variables

The testing variables adopted in this investigation included cement content, water content and curing time for the cemented soils in which GFRP tendons were embedded. It was reported that the compressive strength of cemented soil depends primarily on the water-cement ratio and curing time [1,2,37]. Using the correlation developed between the interface bond strength and cemented soil strength (Fig. 11a), a similar relationship relating reinforcement-soil interface bond strength to the water-cement ratio and curing time could be developed to characterize the effect of the testing variables on the ultimate interface bond strength. The relationship can be expressed as follows:

$$\tau_{p1} = 2662.234 C_w^{-2.415} C_c^{1.984} ln(T_c - 1.851) \qquad (1)$$

where τ_{p1} is the ultimate interface shear strength (bond stress at the first peak of the bond-slip curve); C_w and C_c are water content and cement content, respectively, used in preparing the cemented soil specimen; and T_c is the curing time of the specimen.

Inspection of the trend reflected in Eq. (1), reveals that a water content (C_w) increase in cemented soil leads to an exponential decrease in ultimate bond strength for the soil-reinforcement

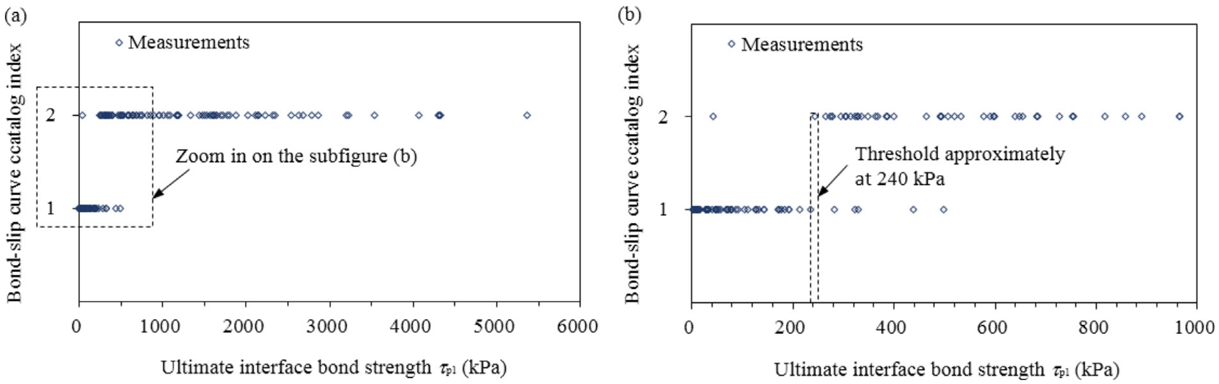

Fig. 12. Switch of bond-slip curve set over increasing ultimate interface bond strength: (a) full range; and (b) close-up range.

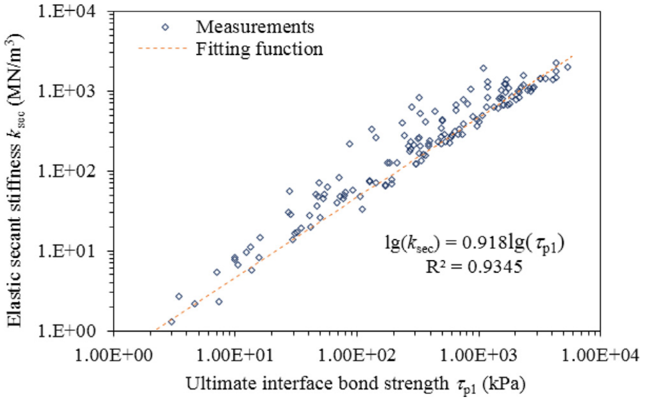

Fig. 13. Correlation associating interfacial secant stiffness and bond strength in elastic phase.

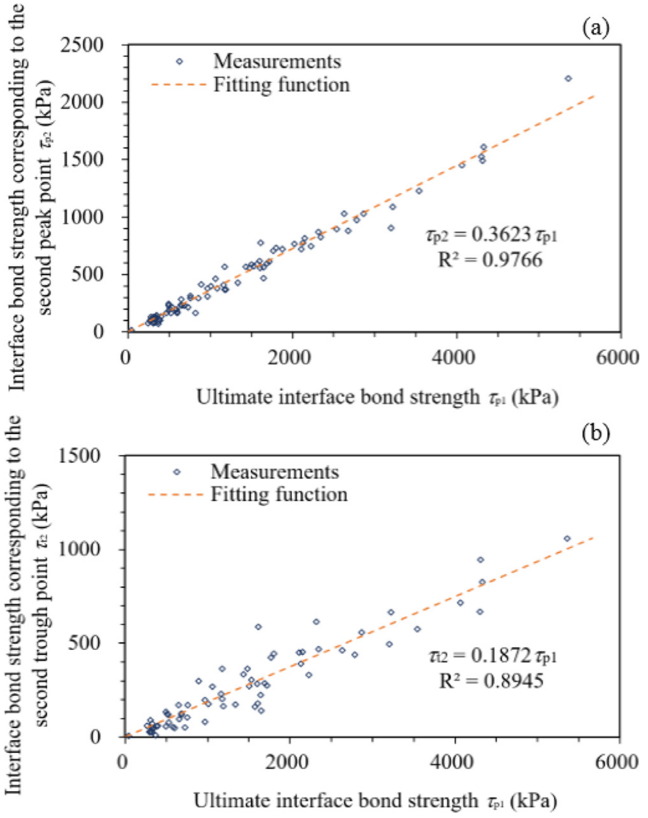

Fig. 14. Bond stress relationship for characteristic points in bond-slip curve: (a) the second peak point versus the first peak point; (b) the second trough point versus the first peak point.

interface, while a cement content (C_c) increase for cemented soil results in an exponential increase in interface bond strength at a comparatively lower rate. Additionally, the interface bond strength increases with increasing curing time (T_c), first at a markedly increasing rate followed by a comparatively small rate after reaching specific curing time values. The trends obtained in this study for GFRP tendons are consistent with those previously identified by Chen et al. (2018a) for steel rebar reinforcement embedded in cemented soils.

The empirical relationship defined by Eq. (1) can be used to predict the value of the ultimate interface bond strength of a typical GFRP tendon embedded in cemented soils, as a function of the corresponding C_w, C_c, and T_c of the cemented soil. Good agreement was observed between the predictions derived from Eq. (1) and the values obtained from tests measuring ultimate interface bond strength, as indicated in Fig. 16. This agreement demonstrates the effectiveness of the proposed ultimate interface bond strength prediction model.

The predictability of the ultimate interface bond strength using the correlation defined in this study (e.g. Fig. 11a and Eq. (1)) can significantly facilitate the design of reinforced cemented soil structures involving GFRP tendons in engineering practice, minimizing or possibly eliminating the need to conduct interface characterization tests or cemented soil compression tests. Note that the extensive application of the above correlations to reinforcement and soil types other than those used in this study still needs more experimental validation.

7. Interpretation of results and load transfer mechanisms

7.1. Simplified interface bond-slip model

Based on the correlations developed in this study for bond stress and slip corresponding to each characteristic point on the bond-slip curve, a piecewise function could be developed to adequately define the interface bond-slip model. The functions corresponding to the different phases the model were established by the coordinates of the end points of their respective segments as indicated in Fig. 9. These segments can be derived from the correlations presented earlier, as follows:

Segment OP$_1$:

$$\tau = \tau_{p1} sin\left(\frac{s}{2s_{p1}}\pi\right) \tag{2a}$$

$$s_{p1} = k_{sec}\tau_{p1} = 10^{-0.918} = 0.12\text{mm} \tag{2b}$$

Segment P$_1$T$_1$:

$$\tau = \frac{\tau_{p1} - \tau_{t1}}{2} cos\left[\frac{s - s_{p1}}{s_{t1} - s_{p1}}\pi\right] + \frac{\tau_{p1} + \tau_{t1}}{2} \tag{3a}$$

$$\tau_{t1} = 0.242\tau_{p1} \tag{3b}$$

$$s_{t1} \approx 9.21 \text{ mm (approximately rib spacing)} \tag{3c}$$

Segment T$_1$ P$_2$:

$$\text{for the waved set}, \tau = \frac{\tau_{t1} - \tau_{p2}}{2} cos\left[\frac{s - s_{t1}}{s_{p2} - s_{t1}}\pi\right] + \frac{\tau_{t1} + \tau_{p2}}{2} \tag{4a}$$

$$\tau_{p2} = 0.362\tau_{p1} \tag{4b}$$

$$s_{p2} \approx 13.29 \text{ mm (approximately 1.5 times rib spacing)} \tag{4c}$$

$$\text{for the still set}, \tau = \tau_{t1} \tag{4d}$$

Segment P$_2$ T$_2$:

$$\text{for the waved set}, \tau = \frac{\tau_{p2} - \tau_{t2}}{2} cos\left[\frac{s - s_{p2}}{s_{t2} - s_{p2}}\pi\right] + \frac{\tau_{p2} + \tau_{t2}}{2} \tag{5a}$$

$$\tau_{t2} = 0.187\tau_{p1} \tag{5b}$$

$$s_{p2} \approx 18.66 \text{ mm (approximately double rib spacing)} \tag{5c}$$

$$\text{for the still set}, \tau = \tau_{t1} \tag{5d}$$

The design of GFRP tendons embedded in cemented soils can be conducted by establishing the interface bond-slip model as shown in Fig. 17: (a) identify the water content (C_w), cement content (C_c) and curing time (T_c) for the cemented soil; (b) identify the rib

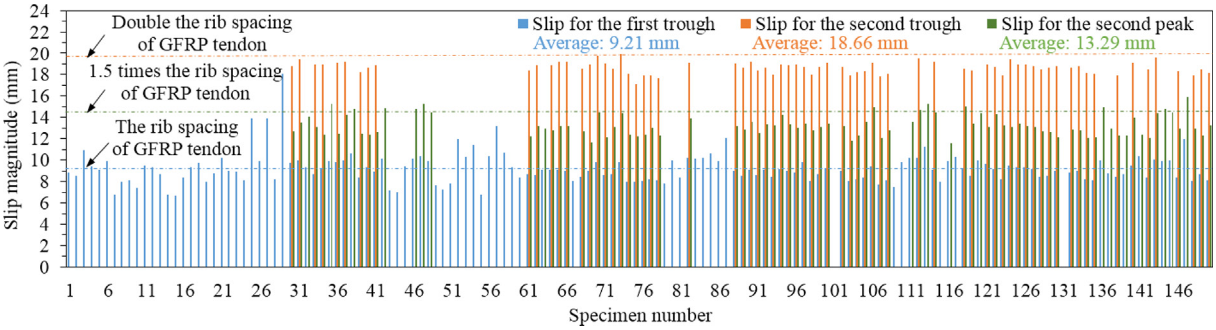

Fig. 15. Slip magnitude for characteristic points in the residual phase.

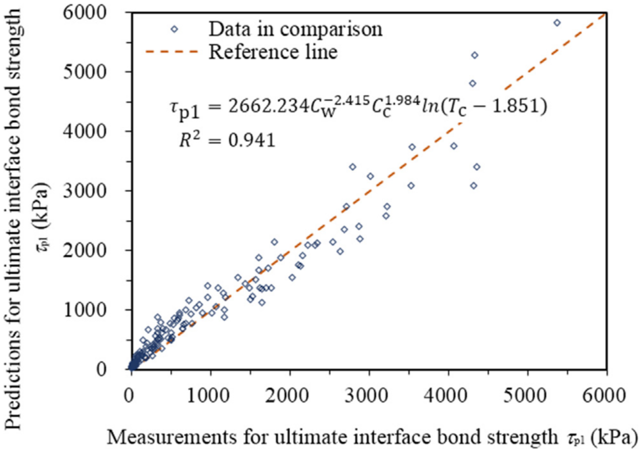

Fig. 16. Evaluation of effectiveness of ultimate interface bond strength prediction model.

spacing for the GFRP tendon; (c) predict the ultimate interface bond strength using Eq. (1); (d) identify the residual phase set type by comparing the estimated ultimate interface bond strength to the bond threshold defined in Fig. 12; (e) predict the interface bond stresses and interface slips corresponding to the characteristic points using the correlations presented in Figs. 11 and 14; (f) using the tendon rib spacing, predict the elastic secant stiffness correlation presented in Fig. 13; (g) complete the piecewise functions for different sections using the estimated bond stresses and slips at the characteristic points and Eqs. (2) through (5).

7.2. Mechanism of interface bond strength mobilization

In this study, observations and information collected from the interface bond-slip curves was used to infer the mechanisms governing the mobilization of bond strength. Load transfer mechanisms that are consistent with the correlations developed in this study can be further assessed by examining dissected specimens as well as the failure patterns observed adjacent to the tendon interface.

Fig. 18 presents schematic representations of the bond mobilization for increasing slip values corresponding to the characteristic points in the interface bond-slip curve. Specifically, Fig. 18a through 18e present the configuration of the GFRP tendon and adjacent cemented soil area for slip values corresponding to the origin, first peak, first trough, second peak and second trough (case of the waved set as depicted in Fig. 9a), respectively. For simplicity, the representations involve an interface segment with only three ribs.

The cemented soil located between ribs of the tendon experiences compressive pressures during pullout-induced movement of the tendon, which is much stiffer than the surrounding cemented soil. The compressive pressures initiate the development of plastic zones within the cemented soil mass, as depicted in Fig. 18a.

With increasing pullout movement of the tendon, the compressive pressures induced at the contact between tendon rib and cemented soil continue to increase until shear failure develops within the soil mass, extending the plastic zone, as illustrated in Fig. 18b. This localized shear failure would result in some interface slip associated with the maximum confinement in the soil and the associated maximum frictional resistance. As a consequence of the mobilized slip, a gap is expected to develop between the cemented soil and the frontal portion of the ribs. Fragments of cemented soil detach from the soil mass, resulting in scratches and subsequent filling of the area between consecutive tendon ribs.

Loose cemented soil continues to accumulate and fill the gap between ribs and possibly resulting in some dilatant behavior such that the soil mass climbs over the back of ribs, leading to a reduction of the effective rib height through which a subsequent cemented soil wedge will travel, as Fig. 18c shows. Upon a slip of magnitude consistent with the rib spacing (9.21 mm), the local confinement on the cemented soil adjacent to the ribs is expected to decrease to its lowest level. This can be attributed to the fact that the gaps between neighboring ribs were maximally filled by the scratched fragments within the travel of the preceding (first) cemented soil wedge. Because that the increased frictional resistance results from increasing local confinement associated with the soil volume filling into the space between ribs, it is reasonable to infer that the volume ratio of cemented soils inside the rib gap corresponding to the residual point (point T_1) and peak point (point P_1) in the bond-slip curve is essentially related to the ratio between the ultimate interface bond strength and residual interface bond strength.

The cemented soil is expected to show a dilatant tendency (i.e. soil climbing over the rib) ultimately resulting in the onset of the residual phase. Due to the reduced height of the rib, in comparison to the original rib height (point P_1), the compression-induced plastic zone and shear failure surface at the second peak (point P_2) are smaller, as illustrated in Fig. 18d. This secondary shear failure occurs when the preceding cemented soil wedge approaches the rib crest along the rib front with a traveling range of approximately 1.5 times the rib spacing.

The space between consecutive ribs are gradually filled by cemented soil fragments from the repeated slippage of cemented soil wedges, resulting in decreasing effective rib height as pullout-induced slippage continues. The difference in space between the remaining rib gap and cemented soil wedge continues diminishing (Fig. 18e), as does the compression developed

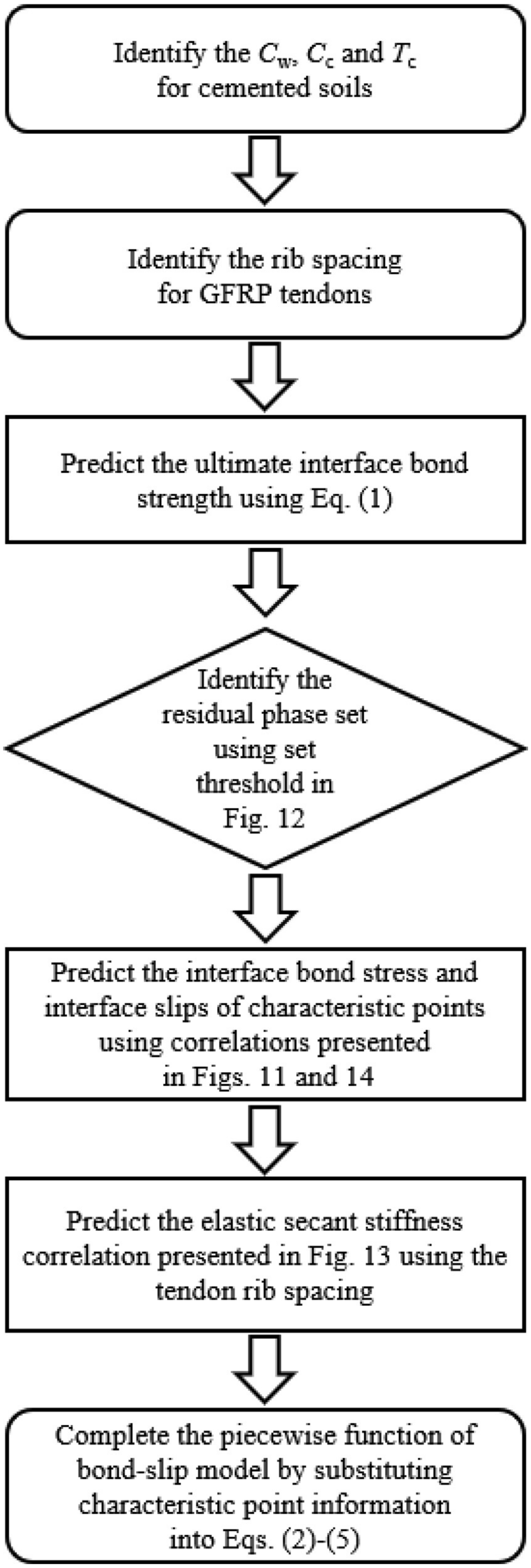

Fig. 17. Procedure of developing bond-slip model for GFRP tendon reinforced cemented soils.

between the preceding wedge and current gap, which corresponds to the remaining bond at the second and following stress trough in the bond-slip curve. It is noteworthy that a cemented soil wedge with comparatively low strength (typically at a compressive strength of 494 kPa) would likely experience initial shear failure in the pullout direction, which would produce an ample volume of fillings in rib gaps. In such a case, the rib-induced interlock effect would disappear in the following travels as rib gaps are completely filled and the cemented soil leads to the development of a comparatively flat profile at the tendon interface. Accordingly, increasing slip develops under constant bond stress, which characterizes the residual phase of the bond-slip curve in the previously defined still set.

8. Conclusions

An experimental study was conducted to characterize the interface bond between GFRP tendons and cemented soil considering varying cement content, water content, and curing time. An element pullout setup was used to conduct tests a unit element reinforced cemented soil specimens. Concurrent unconfined compression tests were conducted on cubic specimens of the cemented soils at conditions corresponding to those used for the pullout specimens. Bond-slip curves of soil-reinforcement interface and unconfined compressive strength of the cemented soils obtained in tests were used to derive correlations relating characteristic bond strengths and testing variables. A piecewise bond-slip model and conceptual description of interface bond mobilization were developed based on the experimental observations and the developed correlations. The following conclusions can be drawn from this investigation:

- The element pullout setup and testing protocols adopted in this study were found capable of providing adequate means for GFRP tendon interface characterization with cemented soil prepared with a predetermined water content, cement content, and curing time.
- The large experimental database generated as part of this study allowed the determination of a bond-slip curve characterized by the presence of a linear phase, a strain-softening phase and a residual phase, which can be represented by a piecewise bond-slip model with piece-end parameters adequately calibrated from the empirically derived correlations.
- The unconfined compressive strength of cemented soils was found to correlate proportionally with the ultimate interface bond strength and can be modeled by a linear relationship. The slopes of the linear relationships were found to reasonably correlate with the tendon surface geometric properties, including rib dimensions and spacing. Specifically, in this study, the magnitude of the slope was found to be 0.486 for the typical GFRP tendon (1.8 mm in rib height and 10 mm in rib spacing).
- The residual interface bond strength, defined as the bond stress corresponding to the first trough point of the bond-slip relationship (i.e., the onset of the residual phase), was found to correlate proportionally with the ultimate interface bond strength and can be modeled by a linear relationship. The slope of the relationship was found to be approximately 0.25.
- The fully softened bond strength was found not to likely be reached within the range of the slip values achieved in the tests conducted in this investigation (slip up to 2 rib spacing equivalents).
- Two typical shapes of bond-slip curves were observed in this study: waved and still. The waved bond-slip curve shape was found to possess a characteristic stress fluctuation in the residual phase, which does not appear in the still bond-slip curve shape where a comparatively constant bond stress (flat) appears in the residual phase. A threshold ultimate interface bond strength of approximately 240 kPa (corresponds to

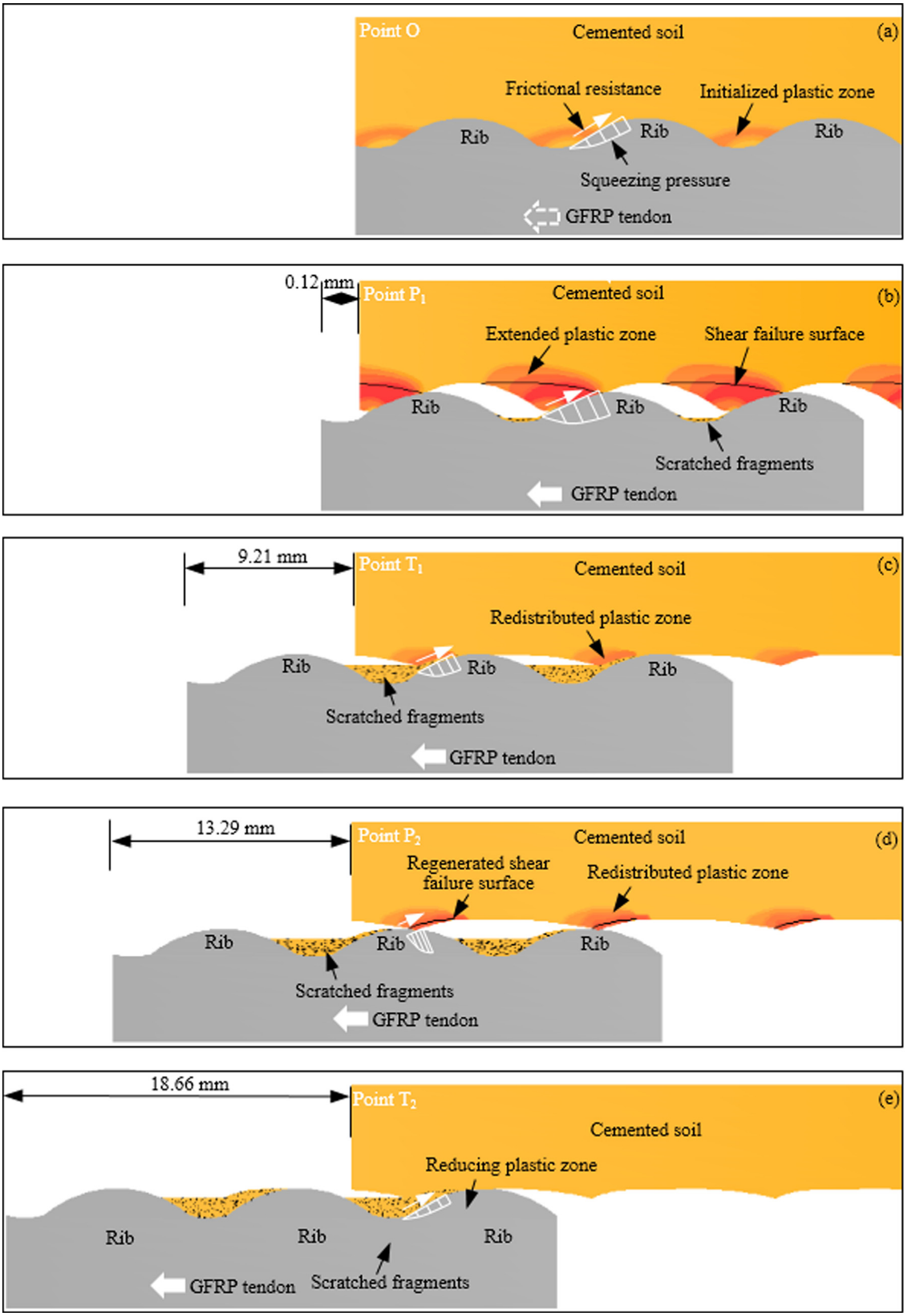

Fig. 18. Bond mobilizing visualization for characteristic points of bond-slip curve: (a) origin O; (b) first peak P_1; (c) first trough T_1; (d) second peak P_2; and (e) second trough T_2.

cemented soil compressive strength of 494 kPa) was found to be separate the tests exhibited the waved and still bond-slip curve shapes. Specifically, a still bond-slip curve shape is likely to observe for tests in which ultimate interface bond strength is

less than 240 kPa, and a waved bond-slip curve shape is likely to observe for tests in which ultimate interface bond strength is greater than 240 kPa.
- The slope of the secant interface shear stiffness corresponding to the peak interface bond was found to correlate exponentially with the ultimate interface bond strength. The obtained correlation depends on the tendon surface properties.
- Three characteristic points involved in the residual phase of the bond-slip curve in the waved bond-slip behavior: (1) the first trough, which corresponds to the onset of the residual phase; (2) the second peak; and (3) the second trough. It was found that the interface bond corresponding to the second peak and second trough are 0.36 and 0.19 of the ultimate bond strength, respectively, for the GFRP tendon used in this study.
- It was found that the slip magnitude corresponding to the first trough (onset of the residual phase) was approximately equivalent to the rib spacing of the GFRP tendon. Also, the slip magnitude corresponding to the second trough was found to be approximately equivalent to twice the rib spacing. Accordingly, as expected, the slip magnitude corresponding to the second peak was found to be approximately equivalent to 1.5 times the rib spacing.
- Ultimate interface bond strength was found to increase exponentially with increasing cement content, decrease exponentially with decreasing water content, and increase with increasing curing time at a decreasing rate.
- The soil-reinforcement interface bond strength can be represented by three components, referred to as mechanical interlock, interfacial friction and interfacial cohesion. The mechanical interlock and interfacial cohesion components were remarkably reduced in the interface bond stress from the peak to the first trough. Thereafter, bond strength tended to consist of gradually decreasing mechanical interlock and constant interfacial friction. The mechanical interlock component was found to substantially contribute to the interface bond strength (approximately 75%) for the typical GFRP tendon used in this study.

Overall, this study provided insights into the interface bond mechanism of GFRP tendons as reinforcement embedded in cemented soils, which are deemed a very competitive substitute to steel reinforcements in ground improvement and earth retention practices involving cement-stabilized soils. Correlations and models developed in this work may substantially facilitate the design of reinforced cemented soil structures by estimating bond strength and stiffness based on the geometry of the tendon and the characteristics of the cemented soil, but without the need of conducting interface characterization tests. However, further physical and numerical modeling on the tendon-matrix interaction is currently undertaken by the authors.

CRediT authorship contribution statement

C. Chen: Project administration, Supervision, Funding acquisition, Conceptualization. **G. Zhang:** Funding acquisition, Conceptualization, Methodology, Data curation, Visualization, Writing - original draft. **J.G. Zornberg:** Writing - review & editing. **A.M. Morsy:** Writing - review & editing. **J. Huang:** Methodology, Investigation, Formal analysis.

Declaration of Competing Interest

The authors declare that they have no known competing financial interests or personal relationships that could have appeared to influence the work reported in this paper.

Acknowledgement

This research was sponsored by the National Natural Science Foundation of China (grants No. 51908201, No. 51978254 and No. 41572298) and State Administration of Foreign Experts Affairs of China (Contract No. G20190018010). The authors appreciate their support.

Appendix A

Measurements obtained in pullout tests and compression tests

Specimen	Compression test				Pullout test								
	UCS_A (kPa)	UCS_B (kPa)	UCS_C (kPa)	UCS_{mean} (kPa)	τ_{p1} (kPa)	s_{p1} (mm)	τ_{t1} (kPa)	s_{t1} (mm)	τ_{p2} (kPa)	s_{p2} (mm)	τ_{t2} (kPa)	s_{t2} (mm)	h_{wed} (mm)
C06W50T07	193.47	179.39	NA	186.43	53.77	1.05	11.02	8.85	NA	NA	NA	NA	6
C06W50T14	180.33	176.40	190.41	182.38	53.23	1.20	23.66	8.50	NA	NA	NA	NA	6
C06W50T28	233.67	206.73	219.18	219.86	70.58	0.85	10.63	10.95	NA	NA	NA	NA	7
C06W50T42	365.31	332.65	377.55	358.50	72.47	1.50	31.83	9.40	NA	NA	NA	NA	10
C06W50T60	340.82	344.90	326.53	337.41	79.31	1.60	36.08	9.10	NA	NA	NA	NA	5
C06W50T90	311.43	296.12	304.69	304.08	92.08	1.60	40.93	9.90	NA	NA	NA	NA	10
C06W60T07	39.18	47.84	NA	43.51	15.75	1.90	8.57	6.80	NA	NA	NA	NA	8
C06W60T14	55.67	53.42	NA	54.54	7.39	3.20	3.41	8.00	NA	NA	NA	NA	10
C06W60T28	72.27	65.25	NA	68.76	13.54	2.40	5.53	8.10	NA	NA	NA	NA	8
C06W60T42	265.31	271.43	NA	268.37	49.09	0.70	20.67	7.40	NA	NA	NA	NA	3
C06W60T60	109.52	104.49	112.45	108.82	49.88	1.90	21.58	9.50	NA	NA	NA	NA	9
C06W60T90	157.14	141.63	151.63	150.14	46.06	0.90	23.71	9.30	NA	NA	NA	NA	7
C06W70T07	67.91	68.57	75.92	70.80	7.02	1.30	2.93	8.70	NA	NA	NA	NA	12
C06W70T14	52.97	55.60	NA	54.29	9.95	1.20	2.49	6.80	NA	NA	NA	NA	0
C06W70T28	76.53	89.18	84.49	83.40	9.95	1.30	2.63	6.70	NA	NA	NA	NA	12
C06W70T42	137.55	124.69	130.20	130.82	30.95	1.90	13.26	8.40	NA	NA	NA	NA	8
C06W70T60	142.64	138.81	139.59	140.35	34.44	1.80	14.55	9.30	NA	NA	NA	NA	13
C06W70T90	162.04	170.41	175.92	169.46	46.63	1.30	19.27	9.70	NA	NA	NA	NA	16
C06W80T07	41.61	43.91	40.13	41.88	10.53	1.60	4.39	8.00	NA	NA	NA	NA	12
C06W80T14	60.71	63.64	60.04	61.46	3.00	2.30	1.36	8.80	NA	NA	NA	NA	7

Appendix A (*continued*)

Specimen	Compression test				Pullout test								
	UCS_A (kPa)	UCS_B (kPa)	UCS_C (kPa)	UCS_{mean} (kPa)	τ_{p1} (kPa)	s_{p1} (mm)	τ_{t1} (kPa)	s_{t1} (mm)	τ_{p2} (kPa)	s_{p2} (mm)	τ_{t2} (kPa)	s_{t2} (mm)	h_{wed} (mm)
C06W80T28	54.69	52.24	51.02	52.65	4.61	2.10	1.73	10.20	NA	NA	NA	NA	11
C06W80T42	59.83	52.80	62.73	58.45	12.39	1.30	2.94	9.00	NA	NA	NA	NA	19
C06W80T60	67.29	73.08	81.37	73.91	16.10	1.10	4.74	8.90	NA	NA	NA	NA	17
C06W80T90	83.40	85.92	89.44	86.26	13.36	1.20	4.75	8.10	NA	NA	NA	NA	13
C06W90T07	47.69	56.93	53.99	52.87	3.46	1.30	0.29	13.90	NA	NA	NA	NA	11
C06W90T14	31.51	30.85	NA	31.18	28.18	0.50	11.05	9.90	NA	NA	NA	NA	8
C06W90T28	71.22	62.86	52.65	62.24	27.52	0.90	5.64	13.90	NA	NA	NA	NA	20
C06W90T42	116.67	117.14	127.35	120.39	28.77	1.00	5.20	8.20	NA	NA	NA	NA	15
C06W90T60	139.02	139.08	130.67	136.26	57.09	0.90	16.15	18.10	NA	NA	NA	NA	11
C06W90T90	126.73	122.65	117.55	122.31	41.84	2.10	14.04	9.70	16.68	12.70	7.02	18.80	12
C12W50T07	917.96	949.80	NA	933.88	386.33	1.88	98.13	10.00	101.08	13.50	55.92	19.40	6
C12W50T14	1139.80	1210.61	1277.14	1209.18	463.54	1.98	140.68	9.29	165.12	14.09	NA	NA	10
C12W50T28	1577.55	1414.69	1414.69	1468.98	647.42	0.97	227.36	8.69	286.48	13.09	171.66	18.99	10
C12W50T42	1651.02	1708.16	1718.37	1692.52	755.99	0.97	264.31	9.29	312.63	12.39	170.52	18.99	10
C12W50T60	1977.55	1742.86	1883.67	1868.03	589.84	2.28	178.24	9.89	196.26	15.29	NA	NA	6
C12W50T90	1946.33	2050.20	2014.29	2003.61	889.72	1.86	389.60	9.78	414.47	12.48	298.42	19.09	8
C12W60T07	618.91	628.99	NA	623.95	265.83	1.29	78.42	10.00	94.86	14.20	59.97	19.20	11
C12W60T14	847.90	809.32	849.16	835.46	277.12	1.19	77.06	10.60	94.15	14.80	NA	NA	9
C12W60T28	960.41	990.61	951.84	967.62	314.72	1.24	71.29	8.35	110.80	12.45	52.50	18.25	8
C12W60T42	922.45	908.16	969.39	933.33	328.26	1.59	102.79	9.30	120.75	12.40	71.84	18.60	8
C12W60T60	942.45	934.45	925.10	934.00	505.89	1.18	176.21	8.89	204.63	12.59	122.21	18.90	10
C12W60T90	1047.55	1105.92	1011.84	1055.10	384.18	1.78	71.51	10.10	112.65	14.90	NA	NA	6
C12W70T07	338.16	367.76	356.33	354.08	77.13	1.70	26.02	7.20	NA	NA	NA	NA	15
C12W70T14	535.92	531.34	537.89	535.05	79.88	1.50	11.94	7.00	NA	NA	NA	NA	15
C12W70T28	584.49	572.45	575.71	577.55	105.62	2.20	15.51	9.40	NA	NA	NA	NA	12
C12W70T42	667.14	644.49	622.04	644.56	244.34	0.89	70.89	10.10	77.06	14.80	NA	NA	9
C12W70T60	645.10	677.35	681.63	668.03	273.12	1.54	75.60	10.35	111.41	15.25	NA	NA	10
C12W70T90	793.27	803.27	852.86	816.46	277.08	1.49	92.26	9.90	128.30	14.50	NA	NA	11
C12W80T07	213.06	213.47	203.27	209.93	29.70	2.15	4.90	7.65	NA	NA	NA	NA	11
C12W80T14	382.56	385.71	385.07	384.45	40.58	1.45	9.55	7.25	NA	NA	NA	NA	5
C12W80T28	376.94	376.33	374.90	376.05	48.03	1.00	7.39	7.80	NA	NA	NA	NA	10
C12W80T42	417.35	447.35	434.08	432.93	132.74	0.40	28.70	12.00	NA	NA	NA	NA	19
C12W80T60	420.82	430.61	412.86	421.43	127.68	1.70	32.07	10.30	NA	NA	NA	NA	13
C12W80T90	458.57	467.96	504.49	477.01	144.09	0.54	36.09	11.45	NA	NA	NA	NA	10
C12W90T07	165.84	152.38	167.08	161.77	32.39	1.90	14.03	6.80	NA	NA	NA	NA	2
C12W90T14	261.28	263.87	257.14	260.76	87.47	0.40	15.79	10.40	NA	NA	NA	NA	17
C12W90T28	321.63	322.04	328.57	324.08	110.92	3.35	23.16	13.15	NA	NA	NA	NA	7
C12W90T42	415.55	417.86	398.95	410.78	172.23	2.69	25.29	10.70	NA	NA	NA	NA	10
C12W90T60	424.16	425.26	438.30	429.24	171.31	2.59	17.41	9.30	NA	NA	NA	NA	8
C12W90T90	444.49	468.57	494.69	469.25	126.67	1.74	27.20	8.35	NA	NA	NA	NA	1
C18W50T07	2481.88	2453.78	2472.69	2469.45	684.58	2.07	204.94	8.69	231.65	12.19	124.54	18.39	7
C18W50T14	2562.05	2615.97	2563.98	2580.66	1504.34	1.84	457.84	8.58	588.66	13.18	272.53	18.89	7
C18W50T28	3422.45	3436.73	3436.73	3431.97	2026.57	2.61	607.44	9.07	763.94	12.97	NA	NA	5
C18W50T42	4138.78	3955.10	4132.65	4075.51	2131.92	2.21	521.56	9.08	774.27	12.77	389.82	18.88	6
C18W50T60	4359.18	4490.68	4446.94	4432.27	2152.95	2.61	610.46	9.07	817.58	13.17	452.39	19.18	7
C18W50T90	4926.53	4955.10	4912.24	4931.29	2347.00	2.00	607.58	8.97	825.35	13.17	467.79	19.18	6
C18W60T07	1454.90	1637.96	NA	1546.43	498.76	1.13	297.01	8.04	NA	NA	NA	NA	9
C18W60T14	2100.20	2038.78	2118.37	2085.78	653.60	1.12	164.99	8.44	227.33	12.74	95.76	18.55	5
C18W60T28	2278.78	2304.08	NA	2291.43	1174.05	1.05	299.82	8.99	369.87	11.69	204.55	18.99	9
C18W60T42	2701.86	2417.91	2524.49	2548.09	1649.57	1.33	279.07	9.79	469.73	14.48	140.92	19.79	8
C18W60T60	3034.69	3139.39	3120.41	3098.16	1530.54	1.49	429.72	8.63	570.31	12.13	305.05	19.04	5
C18W60T90	2904.08	2867.35	2863.27	2878.23	1691.02	1.23	386.52	8.68	596.83	13.08	287.05	18.59	10
C18W70T07	886.94	934.29	875.10	898.78	294.60	1.39	47.69	9.80	79.85	14.40	25.89	19.90	7
C18W70T14	1175.71	1152.65	1143.27	1157.21	347.57	2.19	86.60	8.00	146.87	12.39	46.81	18.10	12
C18W70T28	1232.04	1241.43	1256.12	1243.20	399.04	1.68	94.28	8.00	136.67	12.19	59.68	17.10	11
C18W70T42	1514.29	1489.80	1514.29	1506.12	491.96	1.83	82.42	8.05	183.31	12.34	58.26	17.95	10
C18W70T60	1801.63	1832.24	1775.10	1802.99	532.03	2.28	106.58	8.20	213.72	12.99	77.02	17.90	10
C18W70T90	1928.98	1989.59	2033.27	1983.95	599.07	2.18	88.54	8.10	163.08	12.29	48.76	17.70	9
C18W80T07	512.04	495.71	509.18	505.65	68.49	1.70	18.19	7.80	NA	NA	NA	NA	10

(*continued on next page*)

Appendix A (*continued*)

Specimen	Compression test				Pullout test								
	UCS_A (kPa)	UCS_B (kPa)	UCS_C (kPa)	UCS_{mean} (kPa)	τ_{p1} (kPa)	s_{p1} (mm)	τ_{t1} (kPa)	s_{t1} (mm)	τ_{p2} (kPa)	s_{p2} (mm)	τ_{t2} (kPa)	s_{t2} (mm)	h_{wed} (mm)
C18W80T14	732.45	749.18	752.65	744.76	177.90	1.39	24.22	10.00	NA	NA	NA	NA	11
C18W80T28	753.67	791.63	784.29	776.53	143.42	2.04	26.13	8.35	NA	NA	NA	NA	13
C18W80T42	930.20	930.20	947.76	936.05	306.70	2.49	109.09	10.20	131.63	13.90	91.18	19.10	20
C18W80T60	1024.29	1046.12	1048.16	1039.52	323.36	0.39	101.49	10.15	NA	NA	NA	NA	17
C18W80T90	1114.90	1131.22	1182.04	1142.72	329.27	0.64	100.91	10.25	NA	NA	NA	NA	11
C18W90T07	430.00	443.67	389.39	421.02	183.89	1.44	49.20	10.65	NA	NA	NA	NA	6
C18W90T14	589.03	561.55	609.66	586.75	234.27	0.59	77.18	9.90	NA	NA	NA	NA	22
C18W90T28	761.22	763.27	767.14	763.88	281.17	0.44	47.42	12.05	NA	NA	NA	NA	20
C18W90T42	864.08	842.45	882.65	863.06	326.27	1.99	59.68	9.00	81.00	13.20	27.00	19.00	10
C18W90T60	982.40	911.80	1013.46	969.22	303.74	2.49	46.79	8.50	77.06	12.90	26.34	18.60	9
C18W90T90	1095.10	1081.22	1073.88	1083.40	335.28	2.49	74.90	9.10	133.41	13.59	47.10	19.20	12
C24W50T07	4171.84	4167.35	4189.80	4176.33	1768.69	1.63	555.95	8.58	705.84	12.57	422.41	18.38	7
C24W50T14	4702.04	4782.61	4826.53	4770.39	2317.43	1.50	731.25	9.07	871.05	13.36	615.65	18.67	6
C24W50T28	5918.37	6010.20	6010.20	5979.59	2713.37	2.09	262.50	8.49	547.10	13.28	187.89	17.99	8
C24W50T42	4740.82	4608.16	4651.02	4666.67	3532.53	1.45	295.87	9.19	959.01	14.26	272.91	18.99	2
C24W50T60	6177.55	6234.69	6181.63	6197.96	2785.21	2.58	591.45	8.98	973.21	13.36	438.21	18.88	6
C24W50T90	5840.82	5736.73	5875.51	5817.69	3541.76	2.46	717.32	8.87	1227.29	13.05	574.41	18.98	9
C24W60T07	2550.11	2523.11	2682.77	2585.33	1174.05	0.90	529.58	9.83	566.01	13.43	364.26	18.74	9
C24W60T14	3263.27	3340.82	3287.76	3297.28	1646.52	1.73	358.62	8.08	560.18	12.78	225.12	17.99	4
C24W60T28	3761.22	3638.78	3724.49	3708.16	2110.42	2.11	489.29	8.68	723.19	13.07	451.66	18.68	6
C24W60T42	5214.29	4853.06	4779.59	4948.98	2628.90	2.40	588.30	9.28	1028.82	13.46	463.25	19.08	10
C24W60T60	5163.27	5351.02	5304.08	5272.79	2883.32	2.28	NA	NA	NA	NA	NA	NA	7
C24W60T90	5444.90	5120.41	5071.43	5212.24	2868.55	2.58	629.09	8.97	1026.98	13.16	559.19	18.68	6
C24W70T07	1662.24	1665.51	1634.90	1654.22	494.43	1.43	178.46	8.04	245.75	11.84	134.58	17.94	12
C24W70T14	2293.07	2294.03	2370.17	2319.09	753.74	1.97	173.73	8.19	294.21	12.29	103.67	18.20	9
C24W70T28	2355.71	2399.80	2394.29	2383.27	965.03	2.66	273.18	8.39	377.10	13.59	195.97	18.29	13
C24W70T42	2759.18	2922.45	2830.61	2837.41	1480.38	1.84	409.59	9.38	558.80	14.98	362.78	19.09	12
C24W70T60	3334.69	3365.31	3359.18	3353.06	1571.07	1.94	231.13	7.69	593.91	12.08	160.91	17.79	12
C24W70T90	3608.16	3655.10	3171.43	3478.23	1605.97	2.44	227.78	8.09	556.47	12.78	178.76	18.09	11
C24W80T07	844.90	801.43	820.61	822.31	192.02	2.49	45.84	7.50	NA	NA	NA	NA	11
C24W80T14	1322.57	1260.82	1346.53	1309.97	213.72	1.69	91.80	9.80	NA	NA	NA	NA	10
C24W80T28	1217.96	1222.45	1244.49	1228.30	323.51	1.24	108.65	10.25	127.94	13.55	NA	NA	15
C24W80T42	1955.10	1969.39	2026.53	1983.67	683.24	2.37	171.63	10.19	230.12	14.69	119.37	19.50	13
C24W80T60	2420.20	2391.43	2465.31	2425.65	857.21	0.82	242.83	11.24	292.56	15.24	NA	NA	12
C24W80T90	2504.08	2467.35	2375.51	2448.98	1187.54	1.46	214.25	9.09	370.34	14.49	165.28	19.19	15
C24W90T07	758.57	785.51	800.00	781.36	192.74	2.79	47.28	8.00	NA	NA	NA	NA	3
C24W90T14	1034.78	1064.71	1080.00	1059.83	363.78	0.89	90.38	9.90	88.96	11.60	NA	NA	10
C24W90T28	1296.12	1303.06	1316.12	1305.10	439.46	0.78	78.98	10.30	NA	NA	NA	NA	13
C24W90T42	1607.55	1550.41	1664.69	1607.55	520.62	1.83	108.04	9.25	167.42	15.04	120.28	18.55	15
C24W90T60	1777.14	1635.10	1790.82	1734.35	577.49	2.58	85.66	8.50	193.42	13.39	55.26	18.40	8
C24W90T90	1875.71	1893.27	1906.53	1891.84	597.72	2.18	96.21	10.00	176.97	14.39	NA	NA	13
C30W50T07	4718.49	4955.25	4473.95	4715.90	1804.11	2.62	603.38	9.67	733.74	13.07	443.43	18.98	4
C30W50T14	6734.69	6385.71	6853.06	6657.82	3014.98	2.18	299.82	9.19	456.73	14.28	246.58	18.69	9
C30W50T28	8146.94	7469.39	7469.39	7695.24	3992.32	1.78	198.94	8.24	551.13	13.23	139.80	17.94	6
C30W50T42	8293.88	7593.88	7861.22	7916.33	4303.62	2.44	868.92	9.47	1527.19	13.14	667.05	19.47	12
C30W50T60	9172.27	9451.02	9159.18	9260.82	4332.55	2.97	989.19	9.31	1610.89	13.38	826.17	18.92	8
C30W50T90	9922.45	10383.67	10459.18	10255.10	5363.07	2.69	1454.25	9.34	2207.99	13.21	1059.16	18.96	9
C30W60T07	4130.43	4020.70	4163.56	4104.90	1614.29	1.34	758.83	9.17	775.88	13.07	588.30	18.78	10
C30W60T14	5329.00	5460.08	5378.79	5389.29	2226.53	2.01	504.17	8.48	746.72	12.67	332.48	18.49	7
C30W60T28	6214.29	5783.67	5944.90	5980.95	3221.78	2.27	787.49	8.57	1091.43	12.66	665.91	18.67	8
C30W60T42	7851.02	7457.14	7753.06	7687.07	4312.24	1.92	1244.74	9.05	1489.39	12.14	946.33	18.76	6
C30W60T60	8289.80	7179.59	7877.55	7782.31	4358.19	2.12	NA	NA	NA	NA	NA	NA	5
C30W60T90	9612.24	8644.90	9089.80	9115.65	4063.76	2.93	904.53	8.86	1450.96	12.84	716.20	18.67	5
C30W70T07	2786.35	2392.96	2684.63	2621.32	1010.63	2.46	307.70	8.99	397.89	12.78	175.07	18.79	5
C30W70T14	3683.67	3744.90	3769.39	3732.65	1432.39	2.34	434.83	8.18	565.57	12.08	335.36	18.19	10
C30W70T28	3544.90	3906.12	3616.33	3689.12	1599.84	2.39	466.97	8.13	616.17	12.13	284.60	18.04	8
C30W70T42	4989.80	4848.98	5069.39	4969.39	2541.44	2.50	333.44	9.99	896.65	14.96	NA	NA	9
C30W70T60	5591.84	5436.73	5412.24	5480.27	2680.36	2.69	473.16	8.78	879.12	12.96	NA	NA	6
C30W70T90	5773.47	5759.18	5808.16	5780.27	3203.88	2.28	632.46	8.48	905.64	12.27	495.87	17.88	13
C30W80T07	1489.59	1452.04	1502.86	1481.50	640.16	2.07	173.05	8.69	236.55	12.29	NA	NA	7

Appendix A (*continued*)

Specimen	Compression test				Pullout test								
	UCS_A (kPa)	UCS_B (kPa)	UCS_C (kPa)	UCS_{mean} (kPa)	τ_{p1} (kPa)	s_{p1} (mm)	τ_{t1} (kPa)	s_{t1} (mm)	τ_{p2} (kPa)	s_{p2} (mm)	τ_{t2} (kPa)	s_{t2} (mm)	h_{wed} (mm)
C30W80T14	2656.93	2559.42	2765.01	2660.45	1061.03	2.16	325.81	9.49	461.32	13.98	268.14	19.09	11
C30W80T28	2674.08	2727.14	2761.43	2720.88	1086.54	0.56	373.40	10.39	376.46	12.39	NA	NA	15
C30W80T42	3500.00	3655.10	3551.02	3568.71	1337.34	2.15	237.63	8.39	428.28	12.08	174.08	18.49	8
C30W80T60	3693.88	3683.67	3703.93	3693.83	1717.86	2.54	448.41	10.08	612.62	14.38	274.73	19.59	17
C30W80T90	4079.59	3912.24	3940.82	3977.55	1876.19	2.18	449.92	9.93	722.32	14.82	NA	NA	15
C30W90T07	1420.61	1330.82	1445.51	1398.98	492.88	2.28	176.25	9.99	231.17	14.49	NA	NA	9
C30W90T14	1735.50	1813.03	1758.19	1768.91	367.05	2.34	22.55	8.35	72.28	12.95	8.62	18.35	20
C30W90T28	2340.82	2362.24	2418.78	2373.95	816.56	1.17	142.53	12.00	163.31	15.90	NA	NA	13
C30W90T42	2105.04	2351.02	2744.90	2400.32	727.02	2.52	95.08	8.05	214.45	12.94	52.08	17.95	12
C30W90T60	2780.41	2847.76	2898.37	2842.18	1162.58	1.86	273.55	8.70	407.21	12.30	230.03	18.50	16
C30W90T90	3045.51	3344.49	3460.20	3283.40	965.46	2.21	143.36	8.14	307.19	13.24	81.92	18.15	12

Appendix B

Bond-slip curves for 150 tensioned GFRP tendon specimens in cemented soils, measured in element pullout tests, are presented as follows:

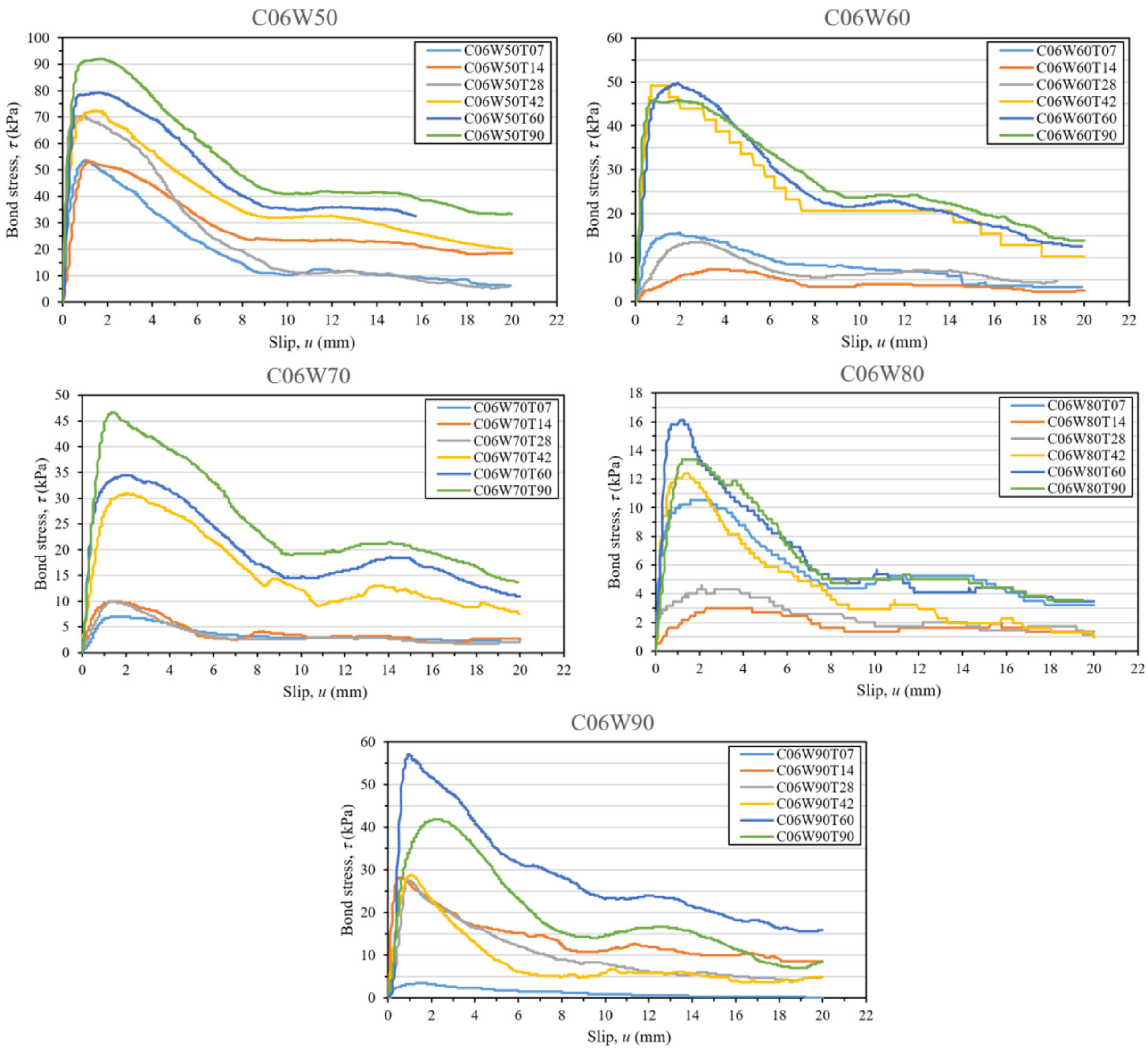

Fig. B1. Bond-slip curves for pullout specimens with 6% cement content.

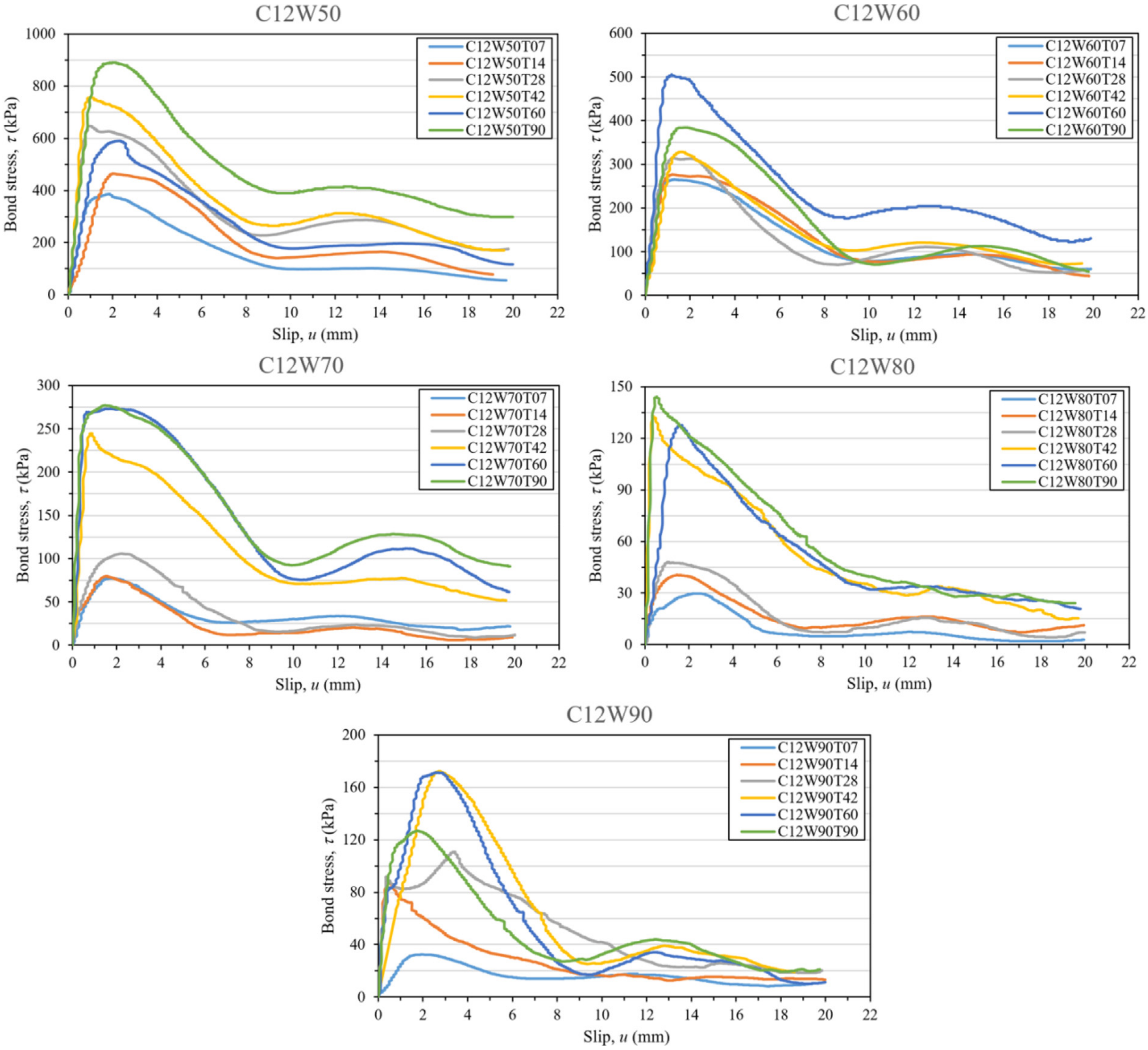

Fig. B2. Bond-slip curves for pullout specimens with 12% cement content.

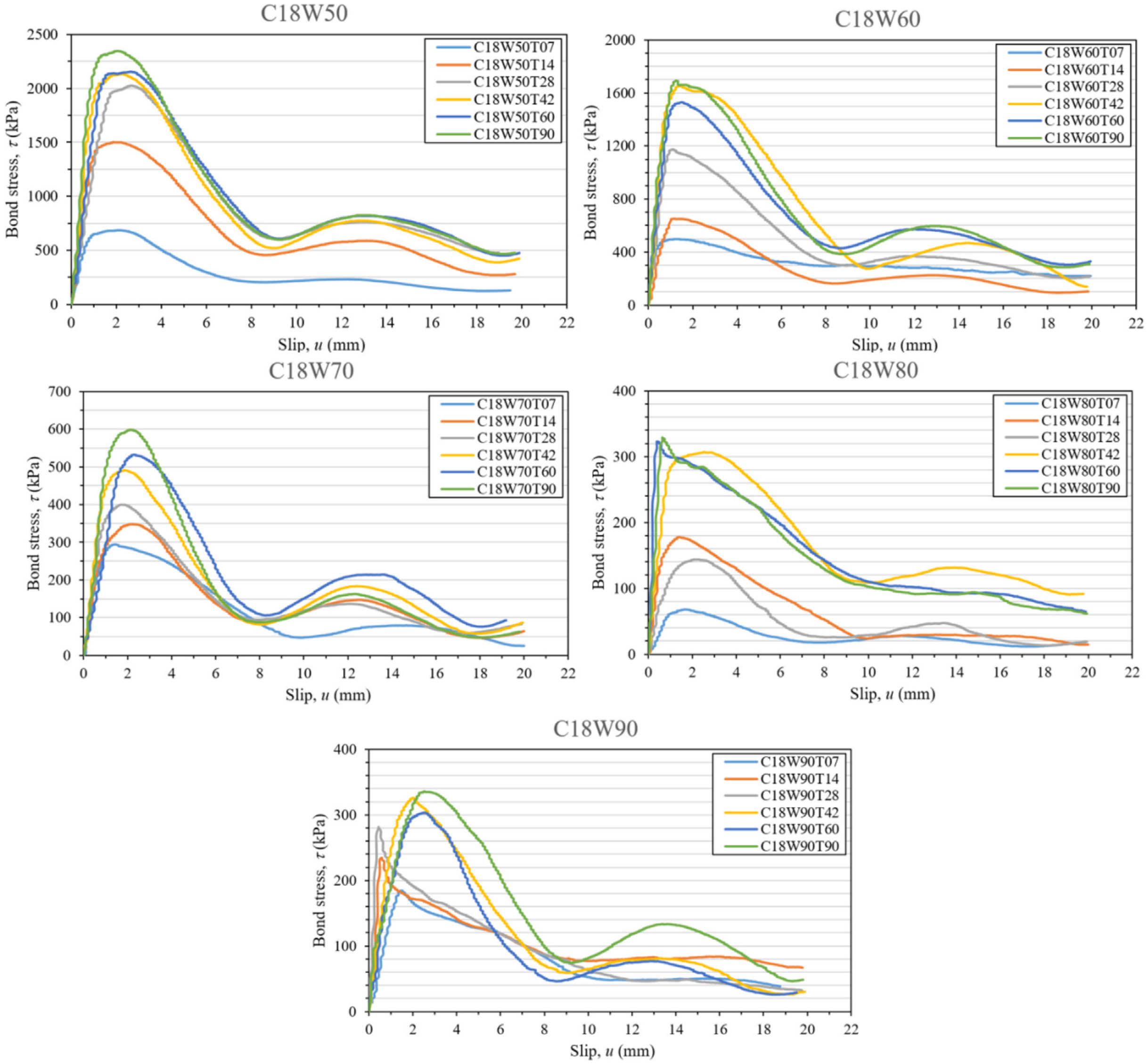

Fig. B3. Bond-slip curves for pullout specimens with 18% cement content.

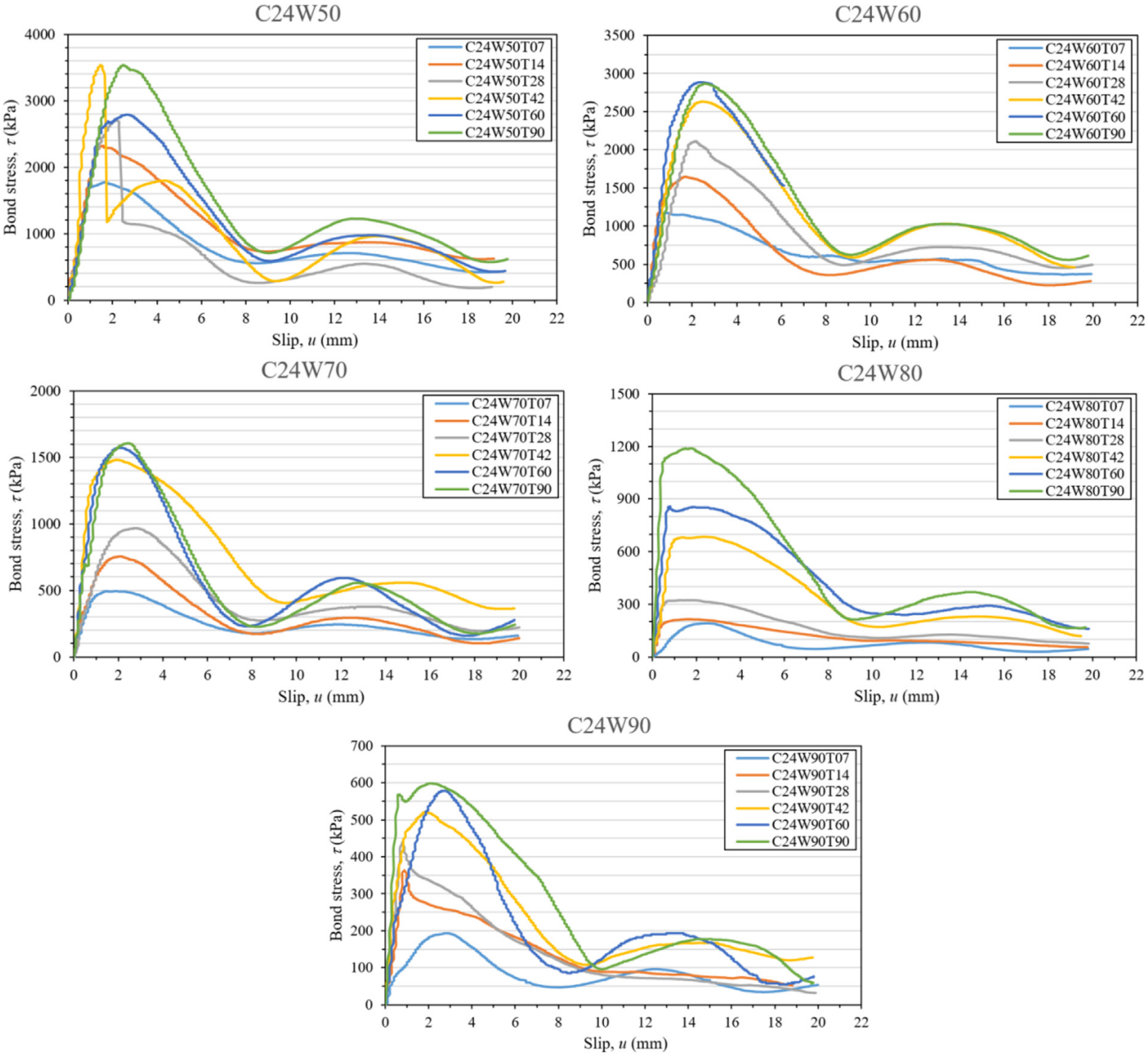

Fig. B4. Bond-slip curves for pullout specimens with 24% cement content.

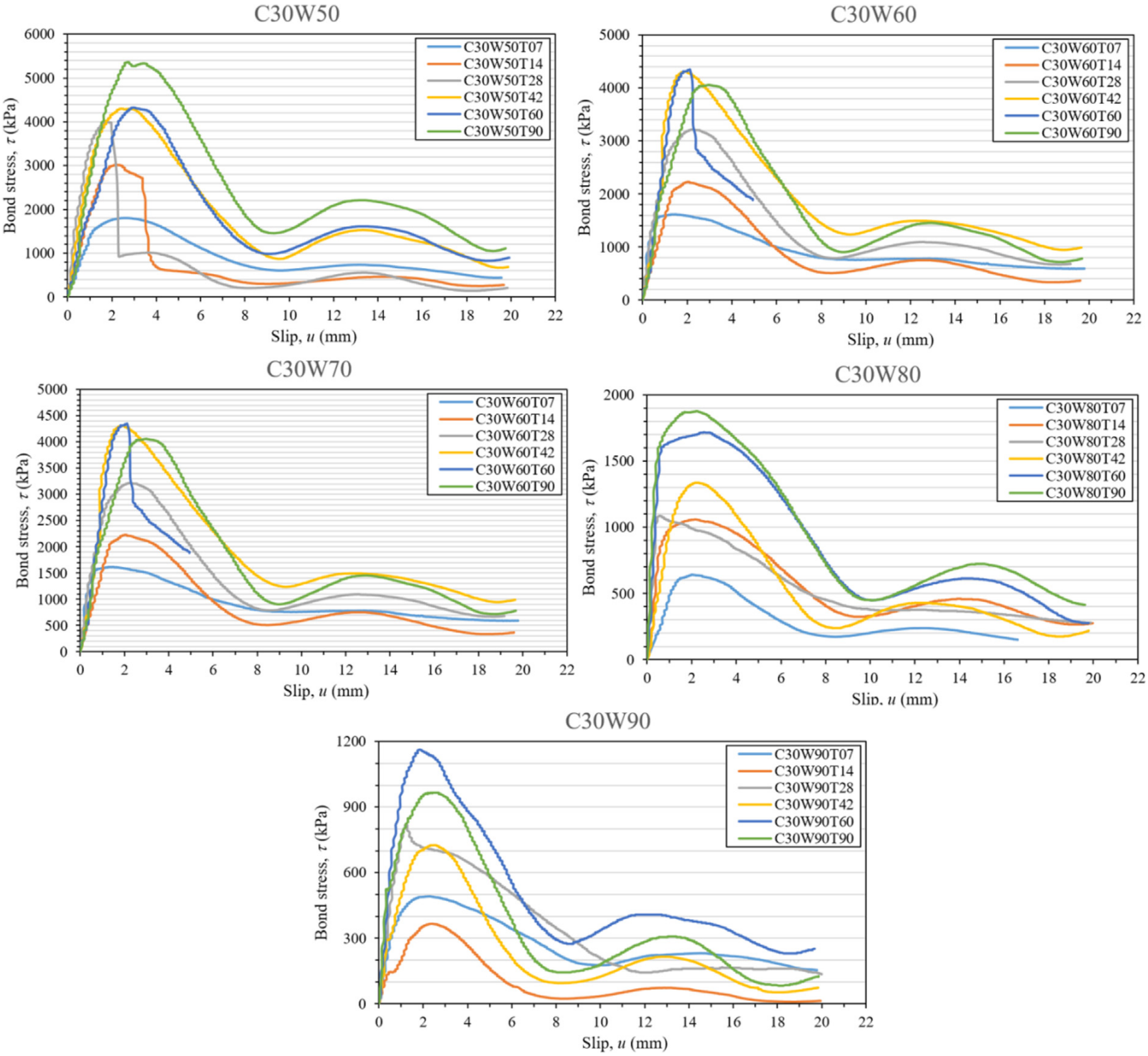

Fig. B5. Bond-slip curves for pullout specimens with 30% cement content.

References

[1] K. Kirsch, A. Bell, Ground Improvement, 3rd ed., CRC Press, Taylor & Francis Group, Boca Raton, Florida, 2013.

[2] J. Han, Principles and Practices of Ground Improvement, John Wiley & Sons, Inc., Hoboken, New Jersey, 2016.

[3] B. Fatahi, H. Khabbaz, B. Fatahi, Mechanical characteristics of soft clay treated with fiber and cement, Geosynth. Int. 19 (3) (2012) 252–262, https://doi.org/10.1680/gein.12.00012.

[4] L.S. Ho, K. Nakari, M. Duc, et al., Analysis of strength development in cement-treated soils under different curing conditions through microstructural and chemical investigations, Constr. Build. Mater. 166 (2018) 634–646, https://doi.org/10.1016/j.conbuildmat.2018.01.112.

[5] H. Xu, L. Chen, J. Deng, Uplift tests of jet mixing anchor pile, Soils Found. 54 (2) (2014) 168–175.

[6] CECS 147, Technical Specification for Soil Mass with Reinforced Cement Soil pile and Anchors, China Planning Press, Beijing, China, 2016.

[7] C. Chen, G. Zhang, J.G. Zornberg, et al., Interface behavior of tensioned bars embedded in cement-soil mixtures, Constr. Build. Mater. 186 (2018) 840–853, https://doi.org/10.1016/j.conbuildmat.2018.07.211.

[8] CEB Task Group Bond Models, Bond of Reinforcement in Concrete, International Federation for Structural Concrete, Lausanne, Switzerland, 2000.

[9] Y. Yun, Y. Wu, W.C. Yang, Performance of FRP bonding systems under fatigue loading, Eng. Struct. 30 (2008) 3129–3140, https://doi.org/10.1016/j.engstruct.2008.04.026.

[10] S.J. Kim, S.T. Smith, Pullout strength models for FRP anchors in uncracked concrete, J. Compos. Constr. 14 (4) (2010) 406–414, https://doi.org/10.1061/(ASCE)CC.1943-5614.0000097.

[11] S.A. Firas, F. Gilles, L.R. Robert, Bond between carbon fiber-reinforced polymer (CFRP) bars and ultra high performance fiber reinforced concrete (UHPFRC): experimental study, Constr. Build. Mater. 25 (2011) 479–485, https://doi.org/10.1016/j.conbuildmat.2010.02.006.

[12] F. Yan, Z. Lin, Bond behavior of GFRP bar-concrete interface: damage evolution assessment and FE simulation implementations, Compos. Struct. 155 (2016) 63–76, https://doi.org/10.1016/j.compstruct.2016.07.078.

[13] F. Yan, Z. Lin, M. Yang, Bond mechanism and bond strength of GFRP bars to concrete: a review, Compos. Part B 98 (2016) 56–69, https://doi.org/10.1016/j.compositesb.2016.04.068.

[14] O. Gooranorimi, W. Suaris, A. Nanni, A model for the bond-slip of a GFRP bar in concrete, Eng. Struct. 146 (2017) 34–42, https://doi.org/10.1016/j.engstruct.2017.05.034.

[15] M. Rezazadeh, V. Carvelli, A. Veljkovic, Modelling bond of GFRP rebar and concrete, Constr. Build. Mater. 153 (2017) 102–116, https://doi.org/10.1016/j.conbuildmat.2017.07.092.

[16] L. Wang, Y. Mao, H. Lv, et al., Bond properties between FRP bars and coral concrete under seawater conditions at 30, 60, and 80℃, Constr. Build. Mater. 162 (2018) 442–449, https://doi.org/10.1016/j.conbuildmat.2017.12.058.

[17] J.D. Frost, J. Han, Behavior of interfaces between fiber-reinforced polymers and sands, J. Geotech. Geoenviron. Eng. 125 (8) (1999) 633–640.

[18] B. Benmokrane, B. Zhang, A. Chennouf, Tensile properties and pullout behavior of AFRP and CFRP rods for grouted anchor applications, Constr. Build. Mater. 14 (2000) 157–170.

[19] B. Zhang, B. Benmokrane, Pullout bond properties of fiber-reinforced polymer tendons to grout, J. Mater. Civ. Eng. 14 (5) (2002) 399–408.

[20] Y.M. Cheng, Y. Choi, A.T. Yeung, et al., New soil nail material—pilot study of grouted GFRP pipe nails in Korea and Hong Kong, J. Mater. Civ. Eng. 21 (3) (2009) 93–102, https://doi.org/10.1061/(ASCE)0899-1561(2009)21:3(93).

[21] Z. Wu, S. Yang, J. Zheng, et al., Analytical solution for the pull-out response of FRP rods embedded in steel tubes filled with cement grout, Mater. Struct. 43 (2010) 597–609, https://doi.org/10.1617/s11527-009-9515-x.

[22] H. Zhu, J. Yin, A.T. Yeung, et al., Field pullout testing and performance evaluation of GFRP soil nails, J. Geotech. Geoenviron. Eng. 137 (7) (2011) 633–642, https://doi.org/10.1061/(ASCE)GT.1943-5606.0000457.

[23] H. Kou, W. Guo, M. Zhang, Pullout performance of GFRP anti-floating anchor in weathered soil, Tunnel. Underground Space Technol. 49 (2015) 408–416, https://doi.org/10.1016/j.tust.2015.06.001.

[24] H. Wang, X. Sun, G. Peng, et al., Experimental study on bond behavior between BFRP bar and engineered cementitious composite, Constr. Build. Mater. 96 (2015) 448–456, https://doi.org/10.1016/j.conbuildmat.2015.07.135.

[25] K. Zhang, Z. Fang, A. Nanni, et al., Experimental study of a large-scale ground anchor system with FRP tendon and RPC grout medium, J. Compos. Constr. 19 (4) (2015) 04014073, https://doi.org/10.1061/(ASCE)CC.1943-5614.0000537.

[26] E.A. Ahmed, E.F. EI-Salakawy, B. Benmokrane, Tensile capacity of GFRP postinstalled adhesive anchors in concrete, J. Compos. Constr. 12(6) (2008) 596–607. http://dx.doi.org/10.1061/(ASCE)1090-0268(2008)12:6(596)

[27] F. Puigvert, A.D. Crocombe, L. Gil, Fatigue and creep analyses of adhesively bonded anchorages for CFRP tendons, Int. J. Adhes. Adhes. 54 (2014) 143–154, https://doi.org/10.1016/j.ijadhadh.2014.05.013.

[28] K. Mei, R. Serocino, Z. Lv, An experimental study on bond-type anchorages for carbon fiber-reinforced polymer cables, Constr. Build. Mater. 106 (2016) 584–591, https://doi.org/10.1016/j.conbuildmat.2015.12.059.

[29] D. Xu, J. Yin, Analysis of excavation induced stress distributions of GFRP anchors in a soil slope using distributed fiber optic sensors, Eng. Geol. 213 (2016) 55–63, https://doi.org/10.1016/j.enggeo.2016.08.011.

[30] Y. Ou, D. Zhu, H. Zhang, et al., Mechanical characterization of the tensile properties of glass fibers and its reinforced polymer (GFRP) composite under varying strain rates and temperatures, Polymers 8 (5) (2016) 196, https://doi.org/10.3390/polym8050196.

[31] N.C. Consoli, D.A. Rosa, R.C. Cruz, et al., Water content, porosity and cement content as parameters controlling strength of artificially cemented silty soil, Eng. Geol. 122 (2011) 328–333, https://doi.org/10.1016/j.enggeo.2011.05.017.

[32] S. Sasanian, T.A. Newson, Basic parameters governing the behavior of cement-treated clays, Soils Found. 54 (2) (2014) 209–224, https://doi.org/10.1016/j.sandf.2014.02.011.

[33] G. Kang, T. Tsuchida, A.M.R.G. Athapaththu, Strength mobilization of cement-treated dredged clay during the early stages of curing, Soils Found. 55 (2) (2015) 375–392, https://doi.org/10.1016/j.sandf.2015.02.012.

[34] C. Chen, G. Zhang, J.G. Zornberg, et al., Element nail pullout tests for prediction of soil nail pullout resistance in expansive clays, Geotech. Test. J. 42 (5) (2018), https://doi.org/10.1520/GTJ20170431.

[35] M. Kitazume, M. Terashi, The Deep Mixing Method, CRC Press, Taylor & Francis Group, Boca Raton, Florida, 2013.

[36] S. Horpibulsuk, N. Miura, T. Nagara, Assessment of strength development in cement-admixed high water content clay with Abrams' law as a basis, Géotechnique 53 (4) (2003) 439–444.

[37] H. Åhnberg, Strength of Stabilized Soils-A Laboratory Study on Clays and Organic Soils Stabilized with Different Types of Binder, PhD Thesis, Lund University, Sweden, 2006.

[38] C.A. Lazarte, H. Robinson, J.E. Gomez, et al., Geotechnical Engineering Circular No. 7, Soil Nail Walls-Reference Manual, Report No. FHWA-NHI-14-007, Federal Highway Administration, Washington, DC, 2015.

[39] B. Benmokrane, A. Chennouf, H.S. Mitri, Laboratory evaluation of cement based grouts and grouted rock anchors, Int. J. Rock Mech. Mining Sci. Geomech. Abstracts 132 (7) (1995) 633–642.

[40] L.B. Martin, M. Tijani, F. Hadj-Hassen, A new analytical solution to the mechanical behavior of fully grouted rockbolts subjected to pull-out tests, Constr. Build. Mater. 25 (2011) 749–755.

[41] S. Ma, J. Nemcik, Z. Aziz, An analytical model of fully grouted bolts subjected to tensile load, Constr. Build. Mater. 49 (2013) 519–526.

[42] R.W. Cooke, G. Price, K. Tarr, Jacked piles in London clay: a study of load transfer and settlement under working Conditions, Géotechnique 29 (2) (1979) 113–147, https://doi.org/10.1680/geot.1979.29.2.113.

[43] R. Yang, J. Zai, The principle of the generalized shear displacement method for analyzing the nonlinear interaction of pile-soil-pile cap, Chin. J. Geotech. Eng. 16 (6) (1994) 103–116.

[44] C. Chen, G. Liang, G. Zhang, et al., A testing system and method for frictional performance of anchor/pile-soil interface, China Patent ZL 2014 1 0176877.6, filed April 29, 2014, and issued March 30, 2016.

[45] C. Chen, G. Liang, X. Liu, et al., A device and method for preparing soil samples used in testing frictional performance of anchor/pile-soil interface, China Patent ZL 2014 1 0176979.8, filed April 29, 2014, and issued July 6, 2016.

[46] Liang G, Chen C, Luo H, et al. A device and method for preparing specimens used in testing frictional performance of anchor/pile-soil interface, China Patent ZL 2014 1 0176977.9, filed April 29, 2014, and issued September 28, 2016.

[47] C. Chen, G. Liang, Y. Tang, et al., Anchoring solid-soil interface behavior using a novel laboratory testing technique, Chin. J. Geotech. Eng. 37 (6) (2015) 1115–1122, https://doi.org/10.11779/cjge201506018.